The contribution of submesoscale over mesoscale eddy iron transport in the open Southern Ocean

Takaya Uchida[1]*, Dhruv Balwada[3], Ryan Abernathey[1,2], Galen McKinley[1,2], Shafer Smith[3], and Marina Lévy[4]

[1]Department of Earth and Environmental Sciences, Columbia University in the City of New York
[2]Division of Ocean and Climate Physics, Lamont-Doherty Earth Observatory
[3]Center for Atmosphere Ocean Science, Courant Institute of Mathematical Sciences, New York University
[4]Laboratoire d'Océanographie et du Climat, Institut Pierre Simon-Laplace

Key Points:

- A state of the art simulation at submesoscale permitting resolution coupled to a full biogeochemical model.
- Mesoscale vertical transport is first-order importance for iron supply from the interior to the surface.
- Submesoscale eddy transport becomes comparable to mesoscale near the surface where mixed-layer instability is active.

*205A Oceanography, Lamont-Doherty Earth Observatory, New York

Corresponding author: Takaya Uchida, takaya@ldeo.columbia.edu

Abstract

In order to examine the roles of ocean dynamics in supplying iron, the limiting nutrient in the open Southern Ocean, to the surface where it can be effectively utilized for photosynthesis, we run a flat-bottom zonally re-entrant channel model configured to represent the Antarctic Circumpolar Current region and couple it to a full biogeochemical model. The model was forced with monthly varying physical and biogeochemical boundary conditions to incorporate seasonality. Much focus on previous studies on iron pathways in the open ocean region has been on mixed-layer entrainment and diapycnal fluxes of iron. The Southern Ocean, however, is a region with strong meso- and submeso-scale turbulence and we would expect eddy fluxes to transport tracers including iron. Spatial resolution is, therefore, chosen as the parameter to control the effect of eddy transport. We utilize cross spectral analysis and the generalized Omega equation to temporally and spatially decompose the vertical transport attributable to meso- and submeso-scale motions. Our results suggest that the mesoscale vertical fluxes provide a first-order pathway for transporting iron across the mixing-layer base where diapycnal mixing is weak and must be included in modelling the open-Southern-Ocean iron budget.

Plain language summary

Ocean currents at the surface on the spatial scales of 1-200 km are energetic due to heating by the sun and stirring by the winds. These currents contribute significantly to the climate system by transporting heat and carbon horizontally towards the poles and vertically into the deep ocean. By running a numerical simulation at very high spatial resolution, we show that these currents are also responsible in transporting iron from the ocean interior to the surface in the Southern Ocean where phytoplankton growth is limited by the lack of iron, a key nutrient for most living organisms on Earth. Our results highlight the importance of accurately representing the ocean currents and associated iron transport in order to understand the Southern Ocean ecosystem and its impact on the climate via photosynthesis, the process in which carbon dioxide is converted to organic carbon and oxygen is produced as a bi-product.

1 Introduction

Ocean turbulence on scales of roughly 1-200 km is characterized by vigorous eddies, fronts, filaments, and other structures which collectively make an important con-

tribution to material transport. These motions can be categorized as either mesoscale or submesoscale depending on their degree of geostrophic balance (McWilliams, 2016). In the context of climate, it is well established that mesoscale transports are of first-order importance to the global ocean heat budget, especially for the vertical transport of heat (Wolfe et al., 2008; Griffies et al., 2015; Liang et al., 2015), and can drive global-scale variations in ocean heat content (Liang et al., 2017; Busecke & Abernathey, 2019). In the Southern Ocean, mesoscale eddies counteract the wind-driven circulation, playing a key role in the climate sensitivity of the global overturning circulation (Farneti et al., 2010; Zika et al., 2013; Gent, 2016).

As observations and simulations resolve smaller and smaller scales, the role of submesoscale in determining large-scale ocean stratification has become a topic of interest. Due to the geostrophic inverse energy cascade (Kraichnan, 1967; Charney, 1971), models that resolve submesoscales tend to have more energetic mesoscales than models with coarser resolution (Capet et al., 2008a, 2008b, 2008c). For instance, Lévy et al. (2010) showed that resolving the submesoscales in a basin-scale general circulation model (GCM) led to significant changes in circulation and stratification compared to lower-resolution runs. A coarse-graining analysis of the transports in their model revealed, however, that the impact of higher resolution on tracer transport was mostly due to more energetic *mesoscale* and large-scale flow, rather than the direct contribution of submesoscales even within the mixed layer (Lévy, Resplandy, et al., 2012, Fig. 7 in their paper). In contrast, a recent study using outputs from global submesoscale permitting general circulation model (GCM) argued that the near-surface vertical heat flux associated with submesoscale turbulence could dominate over the mesoscale on a global scale (Su et al., 2018). The field has evidently not reached a consensus on the relative contributions of the submesoscale vs. mesoscale tracer transport.

Similar ambiguities regarding the role of the submesoscale in ocean ecosystems exist in the biogeochemical literature. Submesoscale features are apparent in surface chlorophyll observations from high-resolution remote sensing data (Mahadevan, 2016; Lee & Kim, 2018). Recent studies have argued submesoscale vertical transport to be an important pathway in supplying nutrients to the euphotic layer (e.g. Lévy, Ferrari, et al., 2012; Levy & Martin, 2013; Mahadevan, 2016; Lévy et al., 2018; Zhang et al., 2019). Precisely isolating the relative contribution of this mechanism, however, has remained challenging since as was noted earlier, submesoscale physics can feed back onto the large-scale

state. Lévy, Iovino, et al. (2012) coined a useful framework for thinking about this problem: in analyzing simulations of increasing resolution, *local effects* are those impacts directly attributable to the newly resolved small scales, while *remote effects* result from changes to the larger-scale flow which occur at higher resolution. In a simulation of a mid-latitude gyre system, Lévy, Iovino, et al. (2012) found that remote effects won out; as resolution was increased, phytoplankton abundance decreased, despite the increase in submesoscale nutrient flux.

The local vs. remote question has important implications for eddy parameterization in coarse-resolution models. If the submesoscale *local* effect proves to be significant, we would either need to resolve the submesoscale dynamics in such models or parametrize the submesoscale effect on nutrient transport in order to get the correct tracer estimates and predictions. On the other hand, if the main impact of submesoscales to enhance mesoscale transports via the inverse energy cascade (a *remote* effect), we may be able to rely on energy backscatter parametrizations which replicate the inverse energy cascade to energize the mesoscale field without explicitly resolving the smallest scales (Jansen et al., 2015; Anstey & Zanna, 2017; Bolton & Zanna, 2019; Bachman, 2019).

In this paper, our aim is to quantify the impact of eddy fluxes on iron transport in the context of the Southern Ocean using idealized submesoscale-permitting simulations of varying resolution by disentangling carefully between *local* vs. *remote* effects. The Southern Ocean is one of the high-nutrient low-chlorophyll oceans (Field et al., 1998; Nolting et al., 1998; J. K. Moore & Abbott, 2000; Arrigo et al., 2008). Artificial fertilization experiments have shown that iron is predominantly the limiting nutrient in the open ocean region (Martin et al., 1990; De Baar et al., 1995; Coale et al., 2004; Aumont & Bopp, 2006). Recognizing the importance of iron in controlling Southern Ocean biomass and the associated biological carbon pump (Lévy et al., 2013), many past studies have attempted to quantify the iron supply, focusing primarily on boundary processes (i.e. aeolian dust, and deposition by glacial melt, bathymetry and hydrothermal vents; Boyd & Ellwood, 2010; Boyd et al., 2012; Nishioka et al., 2013; Wadley et al., 2014). There has, however, been comparatively limited investigation into how ocean dynamics, specifically eddies and fronts, transport iron from the ocean interior (where it is high in concentration) to the surface layer. Conventional focus has been on coastal processes (McGillicuddy et al., 2015; Mack et al., 2017; Jiang et al., 2019), mixed-layer entrainment of iron due to wintertime cooling (Tagliabue et al., 2014; Llort et al., 2015, 2019) and storms (Carranza

& Gille, 2015; Nicholson et al., 2016), mesoscale isopycnal heaving (Swart et al., 2015; Song et al., 2016, 2018), and lateral stirring (d'Ovidio et al., 2015; Ardyna et al., 2017, 2019). To the best of our knowledge, Rosso et al. (2014, 2016) are the only studies that examine the effect of submesoscale dynamics on iron supply to the surface ocean in the open-ocean region of Southern Ocean, but with the geographical coverage limited to the Kerguelen Plateau region and no consideration of the seasonal cycle.

While it would be ideal to quantify eddy iron transport using in-situ observations such as the Argo floats and Geotraces sections (Tagliabue et al., 2014), they lack the spatial and temporal resolution to sufficiently sample mesoscale and submesoscale features (Llort et al., 2018). Satellite observations on the other hand, while having good surface spatial coverage, cannot directly reveal vertical transport. We, therefore, turn to numerical simulations and tackle the local vs. remote question by temporally and spatially decomposing the eddy *iron* fluxes. We accomplish this by applying cross spectral analysis, which allows us to examine the spatial and temporal scales of eddy transport, and the generalized Omega equation (Giordani & Planton, 2000). From the spectral perspective, mesoscale fluxes have larger spatial and longer timescales than the submesoscale. The Omega equation, in contrast, provides a dynamics-based decomposition, decomposing the eddy transport into a mesoscale component in balance with the ageostrophic horizontal flow and a submesoscale componenent associated with higher Rossby numbers (McWilliams, 2016; McWilliams et al., 2019; Chereskin et al., 2019).

In this study, we adopt the flat-bottom zonally re-entrant channel framework developed by Abernathey et al. (2011) and use spatial resolution as the parameter to modulate the eddy effects; we run four cases ranging from mesoscale to submesoscale permitting resolutions: 20 km with and without eddy parametrization, 5 km and 2 km resolution. Although the configuration is a rather strong idealization, it has been successfully employed to investigate tracer transport in the Southern Ocean (Abernathey et al., 2013; Abernathey & Ferreira, 2015). The channel-like idealization is deliberate, as it lets us keep essentially the same mean flow and large-scale nutrient distribution across all simulations. This mitigates the confounding impacts of resolution on the basin-scale circulation reported in the North Atlantic study of Lévy, Iovino, et al. (2012); in their case, primary production decreased with increased resolution largely due to a change in the mean circulation, namely the Gulf Stream separation which has been shown to be sensitive to submesoscale boundary layer processes (Renault et al., 2016; Schoonover et al.,

2017). In contrast, the main potential remote effect of resolution in our simulations is to energize the mesoscale. This setup therefore provides an ideal testbed to quantify the impacts of mesoscale vs. submesoscale transport on phytoplankton ecology. In this study, our focus is on the the resolution- and scale-dependence of physics and the physical drivers for eddy iron transport. A deeper examination of the ecosystem dynamics and overall controls on primary production is left to a companion paper in preparation (hereon U19).

Our paper is organized as follows: We describe the experimental setup briefly in the next section, and the physical results are shown in section 3. Detailed analysis of seasonal dynamics in the context of baroclinic instability and frontogenesis is found in section 3.1, and the generalized Omega equation we use to decompose meso- and submesoscale motion in section 3.2. We show the biogeochemical results in section 4 with the emphasis on eddy vertical iron transport (Section 4.1), which is compared and contrasted with the vertical eddy buoyancy flux. Conclusions are given in section 5.

2 Model description

2.1 Physical setup

The model setup is similar to Balwada et al. (2018) without a topographic ridge, using the hydrostatic configuration of the Massachusetts Institute of Technology general circulation model (MITgcm; Marshall et al., 1997). The channel domain (L_x = 1000 km $\times$ L_y = 2000 km $\times$ H = 2985 m) is flat bottom and zonally re-entrant on a β-plane centered around 49S ($f_0 = -1.1 \times 10^{-4}$ s^{-1}, $\beta = 1.4 \times 10^{-11}$ m^{-1} s^{-1}). The horizontal grids are on a Cartesian coordinate. The runs with 20 km resolution have 40 vertical levels with 10 m near the surface. The 5 km and 2 km runs have 76 vertical levels with 1 m near the surface. Monthly varying sea-surface temperature (SST) relaxation and zonal wind stress are applied at the surface; SST increases from 0°C to 8°C from south to north, and the zonal cosine-squared-shaped wind stress takes its maximum amplitudes between 0.1-0.2 N m^{-2} at the center of the meridional extent and is tapered to zero at the northern and southern 50 km extent of the domain. The exact formulations are given in Appendix A1. The Leith-scheme horizontal (Pearson et al., 2017) and vertical viscosity values of A_h = 2.15 m^2 s^{-1} and $A_\mathrm{v} = 5.6614 \times 10^{-4}$ m^2 s^{-1} are used. We apply no-slip boundary conditions at the channel walls and bottom with the latter

having a quadratic drag, $C_{\mathrm{d}} = 2.1 \times 10^{-3}$. Other parameter values are given in Table A1.

We run four cases: 20, 5 and 2 km horizontal resolution with 20 km run having the case of i) no eddy parametrization, and ii) mixed-layer instability (MLI; Boccaletti et al., 2007; Fox-Kemper et al., 2011) parametrization turned on. The 20 km run was spun up from a state of rest for 200 years and each run with higher resolution was subsequently spun up from the climatology of the lower resolution run until the domain-averaged temperature field reached a statistical equilibrium. Mixed-layer instability is a type of baroclinic instability that feeds off the available potential energy (APE) within the mixed layer and the parametrization restratifies the mixing layer (ML) due to the instability if otherwise resolved (Fox-Kemper et al., 2008; Fox-Kemper & Ferrari, 2008; Fox-Kemper et al., 2011). We show in U19 that the MLI parametrization, intended for restratifying the ML and not for eddy tracer transport, does not enhance vertical tracer transport compared to the non-parametrized run. Considering that 20 km resolution is mesoscale permitting and not resolving (*grey zone*), one may also consider in addition to MLI, turning on the Gent-McWilliams' eddy-induced velocity parametrization (GM; Gent & Mcwilliams, 1990; McDougall & McIntosh, 2001) developed to extract APE due to otherwise resolved mesoscale baroclinic instability. Hallberg (2013), using a two-layer Phillips-type isopycnal model, however showed that the GM parametrization for models in the grey zone acts to suppress the resolved eddies rather than replicate their effects. The suppression of eddy effects was effective in our case as well; turning on GM resulted in steepening of the isopycnals rather than slumping them (not shown). We, therefore, do not have a case with GM turned on. Further details of the physical boundary conditions and parameters are given in A1 and Table A1.

The Rossby deformation radius (R_d) in all resolution runs at the center of the domain is roughly 14 km. The radius was obtained by solving the Sturm-Liouville eigenvalue problem

$$\frac{d}{dz}\Big(\frac{f^2}{N^2}\frac{d\xi}{dz}\Big) = -\kappa^2\xi \tag{2.1.1}$$

where κ corresponds to the Rossby deformation wavenumber and radius is the inverse wavenumber ($R_d = \kappa^{-1}$). $\xi(z)$ is the vertical mode associated with each wavenumber. Equation 2.1.1 is derived from the linearized quasi-geostrophic potential vorticity equation around a state of rest and prescribing a plane-wave solution (Vallis, 2017, Sections 5.8.2, 9.4.3

in their book). We used the seasonal-zonal mean of stratification as the background state. R_d does not change seasonally, since the interior stratification does not have a strong seasonal cycle. The spatial resolution of 2 km is roughly a decade smaller than R_d allowing for partially resolved submesoscale dynamics (Lévy et al., 2018); relative vorticity (ζ) reaches up to three times the local Coriolis parameter indicated by the Rossby number (Ro = $\frac{\zeta}{f}$ where f is the Coriolis parameter; Fig. 1**d**). Idealized models serve as a valuable tool to investigate the physical drivers of seasonality in (sub)mesoscale turbulence (Qiu et al., 2014; Brannigan et al., 2015). To the best of our knowledge, our study is the first idealized modelling study to compare the MLI parametrization with submesoscale permitting simulations that cover the temporal and spatial range allowing for eddy-eddy and eddy-mean flow interaction under seasonal forcings, for which we show the results in section 3.

2.2 Biogeochemical setup

We couple the seasonally resolving physical simulation to the ecosystem model of Gloege et al. (2017), which simplifies the Darwin biogeochemical model (Follows et al., 2007) to the complexity of the two species ecosystem described in Dutkiewicz et al. (2009); there are two phytoplankton (diatoms and small phytoplankton) and two zooplankton functional groups respectively. The general physiology of each phytoplankton species is that diatoms have a faster maximum growth rate but favor conditions with high nutrient concentrations, while the small phytoplankton are more resilient in low nutrient and light environments but have a slower maximum growth rate (Fig. A2). The model considers the full biogeochemical cycle of phosphate, nitrate, silicate, carbon, oxygen and, for the interest of our study, iron, with 31 distinct prognostic tracers advected and diffused by the flow.

Domain-wide nutrient supply (PO_4, NO_3, Fe and SiO_2) is accomplished via a sponge layer at the northern 100 km extent of the domain. These nutrients then freely evolve in the interior following the circulation and biogeochemical cycles. The relaxation profiles for PO_4, NO_3 and SiO_2 were taken from the World Ocean Atlas (WOA) at 45S and then interpolated onto our model vertical grid. We use the monthly climatological products down to 500 m where monthly data is available and append the annual climatology below. Monthly iron profiles were taken from the Biological Southern Ocean State Estimate (BSOSE; Verdy & Mazloff, 2017) as the Geotraces dataset (Tagliabue et al.,

2012, 2014) did not have sufficient temporal and spatial resolution. In an effort to compensate for the lack of dust, glacial and bathymetric sources, we chose 50S of BSOSE, which had higher concentrations than at 45S, but details of the relaxation profiles ultimately did not make a difference in surface concentrations as the spun up interior iron concentration was rather insensitive to the details of the relaxation profile (not shown). The zonal mean of each product for all four nutrients were taken across 50-150E in the Kerguelen Plateau region. Photosynthetically available radiation (PAR) is prescribed at the surface as a meridional linear fit to the monthly-zonal mean of SeaWiFS product between latitudes of 45-60S taking its minimum (maximum) in June (December; Fig. A2**a-c**).

In order to isolate the effects of iron supply by ocean dynamics from depth in the open ocean region, we did not include dust deposition, glacial melt and bathymetric sources. Our ecosystem is consequently iron limited year round (Fig. A3) and pelagic community transition does not occur; diatoms dominate the community year round whereas in the real Southern Ocean, silicate limitation likely comes into play (J. K. Moore et al., 2004; C. Moore et al., 2013; Carranza & Gille, 2015). Due to this dominance by diatoms, our springtime vertically integrated phytoplankton carbon biomass reaches its apex (timing of $\langle \mathrm{C_p} \rangle$ maximum where $\langle \cdot \rangle = \int \cdot \, dz$; Behrenfeld, 2010) in early November, roughly 1-2 months earlier than estimates from biogeochemical (BGC) Argo floats in the Southern Ocean (Appendix B, Fig. B1; Uchida et al., submitted).

Although we believe that it would be possible to further tune the biogeochemical model, parameters tuned for lower resolution runs were not directly applicable to improve the ecosystem in higher resolution runs due to changes in surface iron concentration; vertical eddy iron transport increased and the spring bloom tended to occur earlier in the year with resolution for the same biogeochemical parameters. Since 2-km resolution coupled to a full biogeochemical model is state of the art in terms of resolution, we decreased the growth rates from those used in Dutkiewicz et al. (2009) within the acceptable parameter range of previous studies (e.g. Dutkiewicz et al., 2009; Bennington et al., 2009; Llort et al., 2015; Gloege et al., 2017) as a one-shot attempt to achieve a reasonable spring bloom. The biogeochemical parameter values were then kept identical for all coarser runs with the maximum growth rate for diatoms and small phytoplankton being 0.81 (= 1/1.24) days^{-1} and 0.56 (= 1/1.8) days^{-1} respectively (Table A2). Considering the agreement in magnitude of the seasonal cycle and timing of bloom on-

set occurring around July (Fig. B1), we argue that our model, although idealized, serves as a valuable tool in quantifying the eddy transport of iron and interaction of physics and biogeochemistry at submesoscales, which is the focus of this study.

We spun up the biogeochemistry for another five years after the dynamics had spun up until the domain averaged iron concentration reached a statistical equilibrium for the 20 and 5 km run. For the 2 km run, we spun up the biogeochemistry for the latter 2.5 years of the total spin up simultaneously with the dynamics at which the iron concentration over the meridional extent we analyze ($y \in [600, 1400]$ km) reached statistical equilibrium. Further details of the biogeochemical boundary conditions and parameter values are given in Appendix A2 and Table A2.

3 Physical results

We start by showing a snapshot of the local Ro in the top 300 m for the 2 km run in September 15 representative of austral winter (Fig. 1**a**), and February 15 as representative of austral summer (Fig. 1**b**). The skewness and seasonal difference of the probability density function (PDF) of Ro increases with resolution; the 20 km shows very little seasonality with the winter and summer PDFs overlying on top of each other. Well-formed mesoscale eddies develop year round, and it is clear that winter time has higher Ro values and finer features than in summer (Fig. 1**d**).

The effect of seasonal forcing in temperature and wind stress can be seen in SST and *mixing*-layer depth (MLD) as daily-spatial means in Fig. 2. The resulting SST takes its maximum in February and minimum in September (Fig. 2**a**) consistent with the seasonal cycle in the ACC region of BSOSE (not shown). The MLD is the depth over which isotropic mixing is active due to surface wind stress and diabatic forcing; here we define this highly variable depth as the zonal 99th percentile of the daily-averaged K-profile parametrization (KPP; Large et al., 1994) boundary layer. We argue that it is the *mixing* layer (ML) and not *mixed* layer that is relevant for tracer subduction/obduction as ML is the layer over which mixing is active (Balwada et al., 2018). The MLD averaged over the meridional extent of $y \in [600, 1400]$ km (in order to avoid the channel wall effects) is the deepest during September and shallowest in January (Fig. 2**b**), slightly out of phase with the seasonal cycle of SST during summer. This shows the the ML variability is buoyancy driven and not the winds which take a bi-annual structure (Appendix A1).

We see that as the spatial resolution increases, the ML becomes shallower, which is expected from mixed-layer instability (MLI; explained in further detail in the section below) effectively restratifying the ML. We attribute the 20 km runs having shallower MLD than the 2 and 5 km run over the summer (January, February, March; JFM) to the difference in vertical resolution. Comparing the 20 km and 20 km MLI run, we see the parametrization effectively restratifies the ML; the wintertime MLD maximum shoals roughly 100 m. The SSTs for the two runs, however, are essentially identical, implying that the parallel increase in SST we see with resolution is due to the mesoscale restratification of the interior rather than MLI.

3.1 Mixed-layer instability as the seasonal driver of submesoscale turbulence

It is common to quantify the temporal variability, seasonality in our case, by examining the kinetic energy (KE) of the system (Sasaki et al., 2014; Callies et al., 2015; Rocha et al., 2016; Uchida et al., 2017). We remove the zero-th zonal wavenumber component (i.e. zonal mean) as the deviation in snapshot outputs every 15 days from the mean, viz. $\mathbf{u}' = \mathbf{u} - \overline{\mathbf{u}}$ where the overbar denotes the seasonal and zonal mean. The 15-day interval was chosen as the time scale at which the autocorrelation of daily-averaged horizontal velocity anomaly (u') at the center of the domain crossed zero (not shown); we treat each anomaly field ($\mathbf{u}'$) as an individual realization of the turbulence process in time. We take the zonal Fourier transform of $\mathbf{u}'$ and temporally average them to construct seasonal-mean spectra ($\overline{|\hat{\mathbf{u}}'|^2}$ where $\hat{(\cdot)} = \int (\cdot) e^{ikx}\, dx$ is the zonal Fourier transform). Since our model is a re-entrant channel, all of our wavenumber spectra were taken in the zonal direction, without any tapering applied, using the Python package `xrft` (`https://xrft.readthedocs.io/en/latest/`) and then averaged over the meridional extent of $y \in [600, 1400]$ km. As a reference to our zonal-mean view of the Southern Ocean, the climatological zonal-wavenumber spectra of AVISO geostrophic KE is shown as well using daily-averaged velocity fields sampled every 15 days. The AVISO zonal-wavenumber spectra were taken at latitudes between 50-60S wrapping zonally around the globe and then averaged meridionally assuming a Cartesian plane between those latitudes. The zonal wavenumber KE spectra (Fig. 3) shows three things: i) the mesoscales (O(50 km)) are more energetic for higher resolution runs similar to Capet et al. (2008a, Fig. 6 in their paper), ii) wintertime has higher KE at scales below 25 km, and iii) large scales (wavenum-

bers corresponding to scales above $O(100$ km$)$) have the same order of magnitude as AVISO observations in the SO. Integrating the KE spectra from the 2 km run over scales below 25 km and plotting it against MLD shows that their seasonality is in phase, i.e. high KE with deep ML and visa versa (Fig. 3**b**).

Following Uchida et al. (2017), we quantify the mechanism for the surface KE seasonality through baroclinic instability and frontogenesis. Frontogenesis is a process in which mesoscale stirring generates submesoscale filaments by bringing buoyancy contrasts closer, setting up localized sources for instabilities (McWilliams, 2016) and can be quantified by the frontogenesis function defined as

$$F_s = \mathbf{Q}_s \cdot \nabla_\mathrm{h} b \tag{3.1.1}$$

where $\mathbf{Q}_s = -\left(\frac{\partial u}{\partial x}\frac{\partial b}{\partial x} + \frac{\partial v}{\partial x}\frac{\partial b}{\partial y} + \frac{\partial w}{\partial x}\frac{\partial b}{\partial z},\ \frac{\partial u}{\partial y}\frac{\partial b}{\partial x} + \frac{\partial v}{\partial y}\frac{\partial b}{\partial y} + \frac{\partial w}{\partial y}\frac{\partial b}{\partial z}\right)$ indicating whether the flow field increases or decreases the buoyancy gradients (Hoskins, 1982; Capet et al., 2008b; Brannigan et al., 2015) and was calculated using 15-daily snapshot outputs. Buoyancy was defined using temperature only as we use a linear equation of state with no salinity ($b = \alpha g \theta$).

Figure 4 shows a time-depth Hovmöller diagram of baroclinic available potential energy (APE) conversion rate ($\overline{w'b'}$), frontogenesis function normalized by the magnitude of horizontal buoyancy gradient ($\overline{F_s/|\nabla_\mathrm{h} b|}$), and the root-mean square of vertical velocity for the 5 and 2 km run (we do not show the 20 km run as the amplitudes were orders of magnitude smaller). The amplitude of each increases with resolution, which is expected from better resolved fronts and mixed-layer instability (MLI; Boccaletti et al., 2007) with higher resolution. We see a strong seasonality of $\overline{w'b'}$, an indicator of MLI within the ML. In a spatial mean sense, $\overline{w'b'}$ and $\overline{F_s/|\nabla_\mathrm{h} b|}$ are both positive year round with the latter more surface intensified. This implies that frontogenesis always acts to strengthen the buoyancy fronts on which MLI feeds off, converting APE to KE. Frontogenesis acting to strengthen the fronts over the summer when ML is shallow is consistent with the seasonal cycle of submesoscale turbulence found by Brannigan et al. (2015), but we also find large positive values over the winter, which may be due to different surface forcing conditions and/or eddy-mean flow interaction; Branningan's domain size was too small to allow for any eddy-eddy and eddy-mean flow interactions. The phasing becomes clearer when we take the depth average over the top 100 m of $\overline{w'b'}$ and $\overline{F_s/|\nabla_\mathrm{h} b|}$ with the two in phase with KE (Fig. 3**b**,**c**). This is consistent with Uchida et al. (2017)

who, using outputs from a ocean-atmosphere fully coupled GCM, showed that even partially resolved MLI can modulate seasonality in surface KE.

Based on the the increase in surface KE with resolution (Fig. 3), we hypothesize that MLI in the submesoscale range acts as an energy source for the inverse energy cascade to energize the mesoscales (O(50 km); Charney, 1971; Arbic et al., 2013; Qiu et al., 2014; Barkan et al., 2015; Callies et al., 2016), and forward cascade, which is here represented by the numerical Leith scheme dissipation (Pearson et al., 2017). We quantify this by taking the seasonal and meridional mean of the zonal wavenumber cross spectra of w' and b', and the KE spectral flux

$$\Pi(k) = -\int_{\kappa>k} \mathcal{R}\left[\hat{\mathbf{u}} \cdot (\mathbf{u} \cdot \hat{\nabla}_{\mathrm{h}}\mathbf{u})^{*}\right] d\kappa \tag{3.1.2}$$

where $\mathbf{u}$ is the 15-daily snapshot output of total horizontal velocity. The former allows us to quantify the spatial scales at which APE conversion to KE due to baroclinic instability is active and the latter the direction of KE cascade; in the framework of geostrophic turbulence we would expect KE to cascade upscale ($\Pi < 0$; Charney, 1971; Arbic et al., 2013). As was noted earlier for the zonal-wavenumber KE spectra, the zonal re-entrant configuration allows us circumvent introducing artificial wavenumber modes and spurious errors by tapering, which Aluie et al. (2018) showed by comparing tapered spectral fluxes to their energetically consistent coarse-graining method. In other words, our spectral flux is exact in the zonal dimension.

The APE conversion rate in the surface 200 m takes its maxima at scales O(30 km) for the 2-km run, which coincides with where seasonality in surface KE is apparent (Figs. 3**a**, 5**a**,**b**). Associated with the surface maxima of APE conversion, there is a change in sign in the spectral flux around O(30 km) particularly during winter at scales reaching into higher wavenumbers than in summer and the magnitude increases with resolution (Fig. 5**e**-**h**), consistent with the findings by Capet et al. (2008c); Sasaki et al. (2014). The 5-km run has a much lower APE conversion rate and consequently a weaker KE spectral flux (Fig. 5**c**,**d**,**g**,**h**). This confirms that MLI acts as an energy source for the inverse KE cascade ($\Pi < 0$) particularly during winter with positive values of $w'b'$ (Fig. 5**a**,**b**) at scales around the Rossby deformation radius, resulting in better agreement between AVISO and higher resolution runs in the mesoscale range (Fig. 3**a**). The forward cascade ($\Pi > 0$) at the smallest scales is due to the Leith-scheme viscosity (Bachman et al., 2017). The large signal of inverse KE cascade at scales above O(100 km) is likely coming from the deep mesoscale

baroclinic instability (Fig. 5**a**). We argue in section 4 that accurate representation of mesoscale dynamics is crucial for modulating the eddy iron transport.

3.2 Decomposing the (sub)mesoscales using the Omega equation

With the advent of submesoscale permitting GCMs, the relative importance of submesoscale heat flux over mesoscale has been an active topic of research; Su et al. (2018) argued that on a global scale, submesoscale vertical heat flux could dominate over the mesoscale. Although the zonal-wavenumber cross spectra is already telling that vertical buoyancy flux associated with submesoscale turbulence is significant in our case as well (Fig. 5**a**,**b**), we can further dynamically decompose the transport into its balanced and unbalanced component. Instead of an ad-hoc temporal or spatial filter commonly applied to decompose the fluxes (Uchida et al., 2017; Su et al., 2018), here we use the generalized Omega equation (Giordani & Planton, 2000) to diagnose the vertical flow field in balance with forcing (Molemaker et al., 2010).

The Omega equation is purely diagnostic in a sense that it includes no terms with a time derivative and takes the form

$$N^2\nabla_{\mathrm{h}} w_{\mathrm{b}} + f_0^2 \frac{\partial^2 w_{\mathrm{b}}}{\partial z^2} = \beta \frac{\partial b}{\partial x} + \nabla_{\mathrm{h}} \cdot \mathbf{Q}(\mathbf{u}, b, \Phi) \tag{3.2.1}$$

where $\mathbf{Q}$ is a function of the instantaneous horizontal velocities, buoyancy and pressure for which the exact form will be given in Appendix C. We define the inverted velocity from eqn. 3.2.1 as the balanced motion (w_{b}) and residual from the total vertical velocity as the unbalanced motion ($w_{\mathrm{ub}} = w - w_{\mathrm{b}}$) and here, we simply show a snapshot example of the inversion at the depth of $z = -211$ m (Fig. 6). To first order, the Omega equation behaves as a low-pass filter, as we can see from Fig. 6**a-c** that w_{b} captures the large-scale features in balance with the ageostrophic horizontal velocities (Giordani & Planton, 2000) and w_{ub} the fronts with superposition of waves. It is no surprise that the contribution of w_{ub} is large near the surface and bottom where MLI and boundary layer processes are active, while w_{b} captures most of the variance in the interior (Fig. 6**d**). As a reference, we also show the root-mean square profile of vertical velocity inverted from the quasi-geostrophic Omega equation (w_{qg}; Hoskins et al., 1978). We see that including higher-order ageostrophic terms captures the variance of total vertical velocity to a better extent (compare w_{b} and w_{qg}).

In order to show the scale separation, it is useful to take the wavenumber power spectra of each component. From Fig. 5**a**,**b**, it is apparent that wintertime has higher submesoscale activity so we will focus only on wintertime for the dynamical decomposition. Figure 7**a-c** shows that the balanced motion has higher power at larger scales than the unbalanced motion, with the latter being surface intensified. The decomposition in power spectra is not exact, as there is correlation between the balanced and unbalanced motion, i.e. $\hat{w}^2 = \hat{w}_{\rm b}^2 + \hat{w}_{\rm ub}^2 + 2\hat{w}_{\rm b}\hat{w}_{\rm ub}^*$ but the power spectra of each component is a good qualitative indicator of the scale separation.

For the cross spectra of vertical velocity and buoyancy, however, the decomposition is exact, i.e. $\hat{w}\hat{b'}^* = \hat{w}_{\rm b}\hat{b'}^* + \hat{w}_{\rm ub}\hat{b'}^*$. The total vertical velocity (w) used here for the decomposition is slightly different from w' in Fig. 5**a**,**b** in that the seasonal-zonal mean was not subtracted out as we use the total horizontal velocity, potential temperature and pressure fields in inverting for $w_{\rm b}$ (eqn. 3.2.1); Figures 5**a** and 7**d** differ by the seasonal mean component but we find the difference is negligible as apparent in comparing the two figures. Due to the zonally re-entrant configuration, a temporal mean and zonal mean are statistically equivalent, but the difference indicates that the seasonal mean in the one year of data has a zonal structure. In other words, $w_{\rm ub}$ includes both the unbalanced and seasonal mean motion with the latter likely causing the negative values at depths below 400 m at scales larger than $O(100$ km) in Fig. 7**f** counteracting the mesoscale eddies. The vertical buoyancy flux associated with the unbalanced motion is more surface intensified than the balanced, consistent with our understanding of MLI (Fig. 7**d-f**). The signal at the very surface at scales above $O(100$ km) in $\mathcal{R}[\hat{w}_{\rm ub}\hat{b'}^*]$ is an artifact likely due to the Monotone Piecewise Cubic Interpolation scheme used to interpolate the w and b' fields onto the same monotonic vertical grid as $w_{\rm b}$ in order to diagnose $w_{\rm ub}$. Looking at the vertical profile of each component (Fig. 7**g**), there is a transition around $z = -100$ m from the unbalanced motion to balanced motion being dominant in fluxing buoyancy.

4 Biogeochemical results

The main goal of our study is to examine how eddy iron transport behaves in our seasonally resolving and submesoscale permitting model coupled to a full biogeochemical model. To this end, we solve the governing equation for iron online in MITgcm implemented as part of the two-species biogeochemical model (Section 2.2; Dutkiewicz et

al., 2009)

$$\frac{\partial \mathrm{Fe}}{\partial t} + \nabla \cdot (\mathbf{v}\mathrm{Fe}) = \dot{\mathrm{Fe}} + D_{\mathrm{Fe}} \tag{4.0.1}$$

where the left-hand side is the familiar form of tendency and advection of passive tracers. The first term on the right-hand side ($\dot{\mathrm{Fe}}$) is the source/sink term which comes from primary production and D_{Fe} the diffusion. Since our domain is zonally re-entrant, it is natural to consider zonal-mean quantities, for which we show the zonal-seasonal mean iron budget:

$$\overline{\frac{\partial \mathrm{Fe}}{\partial t}} = -\overline{\frac{\partial}{\partial y}(v\mathrm{Fe})} - \overline{\frac{\partial}{\partial z}(w\mathrm{Fe})} + \overline{\dot{\mathrm{Fe}}} + \overline{D_{\mathrm{Fe}}}. \tag{4.0.2}$$

We have no contribution from zonal advection due to the zonally re-entrant configuration, viz. $\overline{\partial_x(u\mathrm{Fe})} = 0$. In the following analysis, we only consider the meridional extent of $y \in [600, 1400]$ km away from the north/south walls.

In order to put vertical eddy transport into perspective of the other terms in eqn. (4.0.2), we calculate the zonal-seasonal mean iron budget for winter (July, August, September; JAS) and summer (January, February, March; JFM) using daily averaged outputs (Fig. 8). The eddy transport terms were obtained from daily averaged outputs by applying a Reynolds decomposition, i.e. $\overline{\mathbf{v}'\mathrm{Fe}'} = \overline{\mathbf{v}\mathrm{Fe}} - \overline{\mathbf{v}}\,\overline{\mathrm{Fe}}$. It is clear that the vertical eddy transport ($\overline{w'\mathrm{Fe}'}$; red dashed) is of first-order importance for both seasons, particularly during winter when MLI is active, in the budget. The eddy transport reaches deeper into the water column to bring up iron indicated by positive values ($-\partial_z(\overline{w'\mathrm{Fe}'}) > 0$) than the diffusive fluxes ($\partial_z \overline{F}_{\mathrm{diff}}$; blue), in our case due to KPP mixing. The diffusive flux is convergent near the surface, with the KPP mixing transporting iron down the vertical gradients actively generated by the biogeochemical sink at the surface and eddy iron supply from the interior of iron. The net biogeochemical source/sink term ($\overline{\dot{\mathrm{Fe}}}$) is a net sink near the surface year round due to primary production ($\overline{\dot{\mathrm{Fe}}_p}$) overwhelming the source by remineralization ($\overline{\dot{\mathrm{Fe}}_r}$; green dashed). The contribution due to horizontal eddy transport ($-\partial_y(\overline{v'\mathrm{Fe}'})$; red dotted) and mean advection ($-\nabla\cdot(\overline{\mathbf{v}}\,\overline{\mathrm{Fe}})$; red solid) is small compared to the other terms in our simulation.

4.1 (Sub)mesoscale eddy iron transport

Given its dominant role in the budget, from here on we focus on vertical eddy iron transport. Lévy et al. (2001), in the context of an oligotrophic ecosystem in a baroclinically unstable jet, showed that nutrient supply increased with spatial resolution of their

model; vertical nutrient transport increased both along the submesoscale fronts and with mesoscale vertical velocities energized via the inverse energy cascade. As a reminder, we define the former as the *local* and latter as the *remote* effect. By definition, we would expect mesoscale eddy transport to have longer timescales and larger spatial scales than submesoscale transport. Our goal here is to quantify the spatial and temporal scales of eddy iron transport and their relative contributions. We do so by taking the frequency and zonal wavenumber (ω-k) spectra (Fig. 9) of the eddy terms–defined as the deviation in hourly snapshot outputs from the zonal and seasonal mean ($\mathrm{Fe}' = \mathrm{Fe} - \overline{\mathrm{Fe}}$). The ω-k spectra requires model outputs saved at high frequency for which we use hourly snapshot outputs, and buoyancy snapshot fields were only saved every 15 days. We, therefore, do not show the ω-k cross spectra for the buoyancy flux.

The ω-k power spectra of vertical velocity show differences between summer and winter at scales associated with mesoscale turbulence ($O(30$ km$)$, $O(\omega/f) \sim 0.2$) with wintertime having higher power. There is also a signal of internal waves at super-inertial frequencies ($O(\omega/f) > 1$; Fig. 9**a**,**b**). When examining the cross spectra of vertical velocity and iron, however, the signals at high frequency and wavenumber vanish for both winter and summer (Fig. 9**c**,**d**). This implies that at $z = -211$ m depth which is right below the MLD (Fig. 4**d-f**): i) eddy iron transport associated with mesoscale turbulence associated with scales larger than the Rossby deformation radius dominates over submesoscale, and ii) waves associated with super-inertial frequencies contribute to no net iron transport, consistent with the results by Balwada et al. (2018, Fig. 4 in their paper) which found that internal waves are inefficient in transporting passive tracers. The results were qualitatively similar at $z = -180$ m within the wintertime ML where although there was an increase at larger wavenumbers, no increase at super-inertial frequencies in the vertical iron transport (not shown). Comparing the cross spectra of the 2- to 5-km run (Fig. 9**c-f**), it is obvious that the vertical eddy transport is weaker in the latter. We attribute this to the insufficient inverse energy cascade and resulting energetically weak mesoscale field as was discussed in section 3.1.

Following our argument for vertical buoyancy fluxes, we also decompose the iron fluxes using the Omega equation, i.e. $\hat{w}\hat{\mathrm{Fe}}^{*} = \hat{w}_{\mathrm{b}}\hat{\mathrm{Fe}}^{*} + \hat{w}_{\mathrm{ub}}\hat{\mathrm{Fe}}^{*}$. The scale separation is again evident in Fig. 10**a-c** where the unbalanced transport has its maximum at smaller scales. It is interesting to note that the vertical structure of buoyancy and iron transport by the unbalanced motions are quite different. The eddy buoyancy flux is more sur-

face intensified (Fig. **7c**), while the eddy iron flux is strongest between 100 m and 200 m depth. One might question whether the large amplitude in iron transport at high wavenumbers in the unbalanced motion is due to submesoscale turbulence or internal waves (Fig. 10**c**). The ω-k spectra (Fig. 9), however, show no indications of transport in the frequency range of internal waves ($\omega/f > 1$) so we can safely attribute iron transport due to the unbalanced motion to submesoscale turbulence. Returning to the discussion between the *local* and *remote* effect, Fig. 10**d** shows that, below the top 100 m (where the flux is weak), the transport associated with balanced motion (remote) is larger than the unbalanced component (local); however, unbalanced motions still contribute about 1/3 of the total flux at 200 m depth.

5 Discussion and Conclusions

By running a seasonally resolving model at submesoscale permitting resolution configured to represent the zonal-mean view of the Antarctic Circumpolar Current region, our model partially resolves mixed-layer instabilities (MLI; Boccaletti et al., 2007) and generates well formed mesoscale eddies and fronts (Fig. 1). The agreement between surface KE in our model at scales larger than O(100 km) with KE estimates from satellite altimetry observations improves with higher spatial resolution, as seen in the wavenumber power spectra (Fig. 3**a**), likely as a result of a better-resolved inverse energy cascade (Fig. 5; Capet et al., 2008a, 2008b, 2008c; Lévy et al., 2010; Arbic et al., 2013). The domain size of our model has allowed us to partially resolve submesoscale turbulence and the inverse energy cascade associated with it. By coupling the channel model to a full biogeochemical model, we have examined the relative importance of vertical eddy iron transport associated with meso- and submeso-scale turbulence in the open Southern Ocean, where understanding has primarily relied on vertical diffusion and mixing-layer entrainment framework (Bowie et al., 2009; Tagliabue et al., 2012, 2014; Llort et al., 2015, 2019).

In order to quantify the temporal and spatial scales at which eddy transport was dominant, we took the frequency-wavenumber cross spectra of w and Fe. The spectra at depths below the wintertime maximum of MLD (Fig. 9) showed two things: i) most of the vertical transport is at scales larger than the Rossby deformation radius and ii) internal waves contribute to no net transport of iron. The first point already implies that mesoscale turbulence is the dominant contributor to vertical iron transport below the ML (Fig. 8). Considering that different dynamics can have similar spatial and tempo-

ral scales, we further dynamically decomposed the eddy transport into its balanced and unbalanced component using the generalized Omega equation (Giordani & Planton, 2000) based on the assumption that mesoscale turbulence is associated with Rossby numbers smaller than unity (McWilliams, 2016; Lévy et al., 2018). At depths below the mixed layer, we found that the balanced motion accounts for more than half of the total vertical iron transport where as within the mixed layer where stratification is low and MLI is active (Boccaletti et al., 2007), the relative contribution by unbalanced motion increases significantly (Fig 10**d**).

Although our wintertime biogeochemical consumption of iron is within the bounds of observations, it is too low during summer; Ellwood et al. (2008); Bowie et al. (2009) estimate it to be on the order of 100 μmol m^2 yr^{-1} while as it is roughly 35 μmol m^2 yr^{-1} integrating over the top 100 m in our model (Fig. 8**b**; green dotted line). Due to the lack of pelagic community transition, our bloom is too sharp and is insufficiently sustained over the summer (Appendix B, Fig. B1). As the ecosystem is iron limited year round (J. K. Moore et al., 2013), one approach for increasing summer productivity in future work may be to reduce iron requirements for small phytoplankton, viz. have separate iron-to-phosphate ratio per species (Table A2). Although Dutkiewicz et al. (2009), configured to represent the global ecosystem, did not allow for this, it is likely that phytoplankton adaptation has occurred in the Southern Ocean where small phytoplankton should have advantage under low iron concentrations (Tagliabue et al., 2014). Our sharp bloom should not affect our results qualitatively, however, as an increase in summertime biological consumption would result in larger vertical gradients of iron; assuming that mesoscale stirring is related to the background gradient of iron ($w'\mathrm{Fe}' \sim \kappa \frac{d\mathrm{Fe}}{dz}$ where κ here is the eddy diffusivity), mesoscale eddy iron transport would only increase.

Our findings, which emphasize the importance of eddy iron transport, are complimentary to Freilich and Mahadevan (2019, Figs. 6, 7**e** in their paper) in which they show that isopycnal (sub)mesoscale stirring of nutrients increases with resolution. Rosso et al. (2014, 2016), using an idealized biogeochemical model based on an exponential decay rate of iron, also argued for the importance of submesoscale iron transport in the Kerguelen Plateau region. Enhanced submesoscale turbulence in their model occurred due to flow-bathymetric interaction, resulting in a hot-spot of vertical iron transport downstream of the Kerguelen Islands. Away from bathymetric features, however, they showed that submesoscale eddy transport of iron was weak. Balwada et al. (2018) using a sub-

mesoscale permitting zonal re-entrant model with a topographic ridge showed that downstream of the ridge, vertical tracer transport was enhanced at higher frequency and wavenumber. Both studies imply that surface submesoscale turbulence is enhanced due to flow-bathymetric interaction. Since our model has flat bottom, we do not have geographical hot spots of submesoscale turbulence. We argue that in the zonal-mean sense away from bathymetric features in the open Southern Ocean, it is the *local* effect near the surface where MLI is active and *remote* effect, i.e. mesoscale eddies energized through inverse energy cascade, at depths that dominate the eddy iron transport to the surface. In other words, our results suggest that it is first-order importance to get the energetics of the mesoscale field right either through resolving or parametrizing the inverse energy cascade due to submesoscale baroclinic instabilities for estimating iron and tracer transport. Current generation of eddy parametrizations do not incorporate the effect of inverse energy cascade; however, parameterizing this energy transfer is an active area of research (e.g. Kitsios et al., 2013; Jansen et al., 2015; Anstey & Zanna, 2017; Bolton & Zanna, 2019; Bachman, 2019). Due to computational contraints, GCMs at mesoscale permitting resolutions will continue to be invaluable tools to investigate the coupling between physics and biogeochemistry on a global scale.

Based on modelling studies with higher spatial resolution (Molemaker et al., 2010; Smith et al., 2016; Brannigan et al., 2017; Balwada et al., 2018), it is obvious that even at 2 km resolution, which is state of the art coupled to a full biogeochemical model, our turbulent field is not numerically converged; we would expect both the meso- and submesoscale tracer transport to further increase with resolution. It would be interesting to see how the forward cascade of KE due to the transition from geostrophic to three-dimensional turbulence if otherwise resolved on the scales of O(100-1 m), and its non-linear interaction with the mean flow (Molemaker et al., 2005; Levy & Martin, 2013), would impact eddy iron transport in even high-resolution simulations.

Appendix A Model boundary conditions

A1 Physical forcing

The monthly structure of wind stress profile (Fig. A1) inspired by Sinha and Abernathey (2016) takes the mathematical form,

$$\tau(t,y) = \begin{cases} \left(0.15 - 0.05\ \sin\left[\frac{\pi}{3}(t-0.5)\right]\right) \sin^2\left[\pi \frac{y - a/2}{L_y - a}\right] & , a/2 < y < L_y - a/2 \\ 0 & , y \leq a/2 \text{ or } y \geq L_y - a/2 \end{cases} \tag{A1}$$

where L_y is the meridional extent of the domain, $t \in [1, 2, ..., 12]$ for each month and $a = 100$ km. The westerly jet takes its maximum in the meridional center of the domain and tails off to zero towards the boundaries. The SST is relaxed to the profile (Fig. A1),

$$\theta^*(t,y) = \begin{cases} \dfrac{\theta_0 + \Delta\theta \sin\left[\frac{\pi}{6}(t-1)\right]}{0.3L} y & , 0 < y < 0.3L_y \\ \dfrac{1.5}{0.4L}\ \big(y - 0.3L\big) + \theta_0 + \Delta\theta \sin\left[\dfrac{\pi}{6}(t-1)\right] & , 0.3L_y < y < 0.7L_y \\ \dfrac{\theta_2 - \theta_1 + \Delta\theta \sin\left[\frac{\pi}{6}(t-1)\right]}{0.3L}(y - L) + \theta_2 & , 0.7L_y < y < L_y \end{cases} \tag{A2}$$

where $(\theta_0, \theta_1, \theta_2) = (3.25, 4.75, 8)$ °C and $\Delta\theta = 1.75$ °C. Other physical parameters are listed in Table A1.

A2 Biogeochemical forcing

The light, temperature and nutrient limitation to the phytoplankton growth rate are implemented as

$$\mu_i = \mu_{\max_i} \gamma_i^I \gamma_i^T \gamma_i^N \tag{A1}$$

where $\mu_{\max_i}$, γ_i^I, γ_i^T and γ_i^N are the maximum growth rate of phytoplankton i (diatom: $i = 1$, small phytoplankton: $i = 2$) and limitation factors by temperature, light and nutrients respectively. The full equation for the time evolution of phytoplankton is given in Dutkiewicz et al. (2009, eqns. A1-A5 in their paper) and parameter values in Table A2. Each limitation factor takes values between unity and zero ($\gamma \in [0, 1]$) with one meaning optimum conditions for growth. Light limitation is calculated as

$$\gamma_i^I = \begin{cases} \min\left[F_0^{-1}\left(1 - e^{-\kappa_{\text{par}}\text{PAR}}\right)e^{-\kappa_{\text{inh}}\text{PAR}}, 1\right] & , \text{PAR} > 1 \\ 0 & , \text{PAR} < 1 \end{cases} \tag{A2}$$

where PAR is the photosynthetically available radiation in units of [μEin m^{-2} s^{-1}] and

$$F_0 = \frac{\kappa_{\text{par}}}{\kappa_{\text{par}} + \kappa_{\text{inh}}} e^{\frac{\kappa_{\text{inh}}}{\kappa_{\text{par}}} \log\left[\frac{\kappa_{\text{inh}}}{\kappa_{\text{par}} + \kappa_{\text{inh}}}\right]}.$$

Parameter	Value	Units
Horizontal resolution	20, 5, 2	km
Time step	1800, 150, 40	s
Spin up	200, 35 (from 20 km), 4.5 (from 5 km)	years
SST relaxation piston velocity	1/3	m day^{-1}
Redi diffusivity	200	m^2 s^{-1}
*Typical ML frontal width (L_f)	2	km
*MLI efficiency (C_e)	0.07	
*MLI time scale (τ)	2×10^{-6} (5.8)	s^{-1} (day)
*Maximum grid-scale ($L_{\max}$)	110	km

Table A1. Physical parameter values for each resolution. The piston velocity is defined as the top grid cell height divided by the relaxation time scale. The parameters with (*) are only used for the 20 km run with MLI parametrization turned on. Further information on other variables will be left to Balwada et al. (2018, Supplementary Material Table 1).

Figure A2**d**,**e** shows behaviour of γ^I and $\mu_{\max}\gamma^I$ in the range of PAR used in our model; the light limitation factors (γ^I) are in the range of values presented by Dutkiewicz et al. (2009, Fig. 1**e** in their paper. Note the difference in the units; 10 Ein m^{-2} d^{-1} corresponds roughly to 116 μEin m^{-2} s^{-1}.). The temperature limitation is kept the same for both phytoplankton species and takes a similar formulation to the Arrhenius equation (e.g. Geider, 1987; Brown et al., 2004; Kremer et al., 2017)

$$\gamma_i^T = T_0 \max[e^{-T_{\mathrm{Ae}}\left(\frac{1}{T+T_{\mathrm{kel}}}-\frac{1}{T_{\mathrm{ref}}}\right)}, 10^{-10}] \tag{A3}$$

where T is the local temperature in Celsius and the reference temperature T_{ref} defines the temperature at which $\gamma^T = T_0$. Lastly, the nutrient limitation factor is defined by the most limiting nutrient

$$\gamma_i^N = \min(N_{ij}^{\lim}) \tag{A4}$$

where $N_{ij}^{\lim} = \frac{N_j}{N_j + \kappa_{N_{ij}}}$ with N_j and $\kappa_{N_{ij}}$ being the concentration of nutrient j and half-saturation constant of nutrient j for phytoplankton i respectively. Figure A3 shows that $N_{i\mathrm{Fe}}^{\lim}$ is always smallest amongst the nutrient limitation factors per phytoplankton, viz. $\gamma_i^N = N_{i\mathrm{Fe}}^{\lim} = \frac{\mathrm{Fe}}{\mathrm{Fe}+\kappa_{i\mathrm{Fe}}}$, with a large dip during Oct.-Dec. when the climax of spring bloom takes place. We also see the effect of diatoms having larger half saturation constants; $N^{\lim}$ is lower for diatoms than small phytoplankton for each nutrient year round. Further details of the variables and notations will be left to Dutkiewicz et al. (2009), which the reader should refer to.

Appendix B Seasonality in phytoplankton biomass

The resulting seasonal cycle of vertically integrated phytoplankton biomass ($\langle \mathrm{C_p} \rangle$) is shown in Fig. B1 along with estimates from biogeochemical (BGC) Argo floats deployed by the SOCCOM and SOCLIM projects (Johnson et al., 2017; Riser et al., 2018; Leymarie et al., 2018), and surface biomass concentration ($\mathrm{C_p}$) from the carbon-based production model (CbPM; Westberry et al., 2008). Details of the BGC-Argo float dataset and quality control will be left to Uchida et al. (submitted). The apex of the spring bloom ($\langle \mathrm{C_p} \rangle$ maximum) in our 2 km run occurs roughly 1-2 months earlier than the Argo estimates (Fig. B1**a**,**c**,**e**), which is likely due to the over dominance of diatoms in our ecosystem. The basin-wide maximum of $\langle \mathrm{C_p} \rangle$, however, aligns meridionally with where our ACC lies, indicated by the maximum in KE (Fig. B1**b**). This is consistent with the Argo estimate between 45S-60S (Fig. B1**c**,**d**). The maximum in KE around 40S is due to the Agulhas Current and downstream of the Drake Passage. Although we only analyze the meridional extent of $y \in [600, 1400]$ km in our study, it is also interesting to note the indention in the southward progression of apex around $y \sim 300$ km (Fig. B1**a**), which is likely due to our cosine-squared form of wind stress (eqn. A1); the ML shoals towards the north and south boundaries (Fig. B1**b**). The ML at the very south is deep due to year-round convection at the boundary wall.

Appendix C Omega equation

The right hand side of eqn. 3.2.1 is $\mathbf{Q} = \mathbf{Q}_{\mathrm{tw}} + \mathbf{Q}_{\mathrm{da}}$ where

$$\mathbf{Q}_{\mathrm{tw}} = -2\Big(\frac{\partial \mathbf{u}}{\partial x} \cdot \nabla b, \frac{\partial \mathbf{u}}{\partial y} \cdot \nabla b\Big) \tag{C1}$$

$$\mathbf{Q}_{\mathrm{da}} = f\Big(\frac{\partial v}{\partial x}\frac{\partial u_{\mathrm{a}}}{\partial z} - \frac{\partial u}{\partial x}\frac{\partial v_{\mathrm{a}}}{\partial z}, \frac{\partial v}{\partial y}\frac{\partial u_{\mathrm{a}}}{\partial z} - \frac{\partial u}{\partial y}\frac{\partial v_{\mathrm{a}}}{\partial z}\Big) \tag{C2}$$

Parameter	Symbol	Value	Units
Phytoplankton max. growth rates	$\mu_{\max_{(1,2)}}$	1/1.24, 1/1.8	days^{-1}
Mortality rates	$m_{P_{(1,2)}}$	15, 12	days
	$m_{Z_{(1,2)}}$	40, 40	days
Zooplankton max. grazing rates	$g_{\max_a}$	2.8	days
	$g_{\max_b}$	16.8	days
Half-saturation constants	$\kappa_{\mathrm{PO_4}_{(1,2)}}$	0.035, 0.015	mmole m^{-3}
	$\kappa_{\mathrm{NO_3}_{(i)}}$	$\kappa_{\mathrm{PO_4}_{(i)}} \times r_{\mathrm{N:P}}$	mmole m^{-3}
	$\kappa_{\mathrm{Fe}_{T(i)}}$	$\kappa_{\mathrm{PO_4}_{(i)}} \times r_{\mathrm{Fe:P}}$	mmole m^{-3}
	$\kappa_{\mathrm{Si}_{(1)}}$	$\kappa_{\mathrm{PO_4}_{(1)}} \times r_{\mathrm{Si:P}}$	mmole m^{-3}
Phytoplankton elemental ratios	$r_{\mathrm{N:P}}$	16	
	$r_{\mathrm{Si:P}}$	16	
	$r_{\mathrm{Fe:P}}$	10^{-3}	
PAR saturation constants	$\kappa_{\mathrm{par}_{(1,2)}}$	0.018, 0.01	$(\mu\text{Ein m}^{-2}\ \text{s}^{-1})^{-1}$
PAR inhibition constants	$\kappa_{\mathrm{inh}_{(1,2)}}$	1.05×10^{-3}, 5.9×10^{-3}	$(\mu\text{Ein m}^{-2}\ \text{s}^{-1})^{-1}$
Normalization constant	T_0	0.589	
Activation temperature	T_{Ae}	4040	K
Absolute zero temperature	T_{kel}	273.15	K
Reference temperature	T_{ref}	277.15	K
Nutrition relaxation time scale		30	days

Table A2. The two-species Darwin parameter values used in our configuration where $i(= 1, 2)$ correspond to Diatoms which have an additional silicate dependence and small phytoplankton respectively. In Dutkiewicz et al. (2009), the units of the half-saturation constants are in [μM] (micromole per liter), equivalent to [mmole m^{-3}].

Assuming the total flow to be in geostrophic balance ($\mathbf{u} = \mathbf{u}_\mathrm{g} = \frac{\hat{z}}{f} \times \nabla_\mathrm{h}\Phi$) reduces eqn. (3.2.1) to the quasi-geostrophic Omega equation (Hoskins et al., 1978). The ageostrophic velocities were defined as the difference between the total and geostrophic velocity, i.e. $\mathbf{u}_\mathrm{a} = \mathbf{u} - \mathbf{u}_\mathrm{g}$. We have neglected the terms $\mathbf{Q}_\mathrm{th}$ and $\mathbf{Q}_\mathrm{dm}$ in Giordani and Planton (2000), which correspond to dissipation due to Leith viscosity (Bachman et al., 2017), KPP (Large et al., 1994) and/or bottom drag in our case as we use snapshot outputs to invert eqn. (3.2.1). We find the Omega equation performs well enough for our purpose of decomposing the flow without incorporating these terms (Fig. 6).

We solve for eqn. (3.2.1) in the horizonal wavenumber Fourier space at each vertical level and time, i.e.

$$-\kappa^2 N^2 \hat{w} + f_0^2 \frac{\partial^2 \hat{w}}{\partial z^2} = ik\beta\hat{b} + (ik\hat{Q}^x + il\hat{Q}^y) \tag{C3}$$

where $\kappa = (k, l)$ is the horizontal wavenumber vector using the `xomega` Python package we developed (`https://xomega.readthedocs.io/en/latest/`).

Acknowledgments

This research was supported by NASA Award NNX16AJ35G as part of the SWOT Science Team. Abernathey acknowledges additional support from NSF Award OCE-1553593. The model configuration is available on Github (`doi:10.5281/zenodo.3266400`) and simulation outputs for 15-daily snapshot and monthly averaged outputs of physical variables ($\mathbf{v}, \theta, \Phi$) are available on Pangeo (`https://pangeo-data.github.io/pangeo-datastore/master/ocean/channel.html`). For other variables, please contact the leading author. The World Ocean Atlas data was acquired via `https://data.nodc.noaa.gov/thredds/dodsC/woa/WOA13/DATA/`, BSOSE via `http://sose.ucsd.edu/bsose_solution_Iter105.html`, and SeaWiFS PAR data via `https://oceandata.sci.gsfc.nasa.gov/SeaWiFS/Mapped/Daily/9km/par/`. BGC-Argo data were collected and made freely available by the Southern Ocean Carbon and Climate Observations and Modeling (SOCCOM) Project funded by the National Science Foundation, Division of Polar Programs (NSF PLR -1425989), supplemented by NASA, the Southern Ocean and Climate Field Studies with Innovative Tools (SOCLIM) Project funded by the Foundation BNP Paribas and the Massachusetts Water Resource Authority, and by the International Argo Program and the NOAA programs that contribute to it. (`http://www.argo.ucsd.edu`, `http://argo.jcommops.org`). CbPM data was acquired via the Oregon State University web portal (`http://orca.science.oregonstate.edu/1080.by.2160.8day.hdf.carbon2.m.php`).

References

Abernathey, R., & Ferreira, D. (2015). Southern ocean isopycnal mixing and ventilation changes driven by winds. *Geophysical Research Letters*, *42*(23).

Abernathey, R., Ferreira, D., & Klocker, A. (2013). Diagnostics of isopycnal mixing in a circumpolar channel. *Ocean Modelling*, *72*, 1–16.

Abernathey, R., Marshall, J., & Ferreira, D. (2011). The dependence of southern ocean meridional overturning on wind stress. *Journal of Physical Oceanography*, *41*(12), 2261–2278.

Aluie, H., Hecht, M., & Vallis, G. K. (2018). Mapping the energy cascade in the north atlantic ocean: the coarse-graining approach. *Journal of Physical Oceanography*, *48*(2), 225–244.

Anstey, J. A., & Zanna, L. (2017). A deformation-based parametrization of ocean mesoscale eddy reynolds stresses. *Ocean Modelling*, *112*, 99–111.

Arbic, B. K., Polzin, K. L., Scott, R. B., Richman, J. G., & Shriver, J. F. (2013). On eddy viscosity, energy cascades, and the horizontal resolution of gridded satellite altimeter products. *Journal of Physical Oceanography*, *43*(2), 283–300.

Ardyna, M., Claustre, H., Sallée, J.-B., D'Ovidio, F., Gentili, B., Van Dijken, G., ... Arrigo, K. R. (2017). Delineating environmental control of phytoplankton biomass and phenology in the southern ocean. *Geophysical Research Letters*, *44*(10), 5016–5024.

Ardyna, M., Lacour, L., Sergi, S., dOvidio, F., Salle, J.-B., Rembauville, M., ... Claustre, H. (2019). Hydrothermal vents trigger massive phytoplankton blooms in the southern ocean. *Nature Communications*, *10*, 2451.

Arrigo, K. R., van Dijken, G. L., & Bushinsky, S. (2008). Primary production in the southern ocean, 1997–2006. *Journal of Geophysical Research: Oceans*, *113*(C8).

Aumont, O., & Bopp, L. (2006). Globalizing results from ocean in situ iron fertilization studies. *Global Biogeochemical Cycles*, *20*(2).

Bachman, S. D. (2019). The gm+ e closure: A framework for coupling backscatter with the gent and mcwilliams parameterization. *Ocean Modelling*.

Bachman, S. D., Fox-Kemper, B., & Pearson, B. (2017). A scale-aware subgrid model for quasi-geostrophic turbulence. *Journal of Geophysical Research:*

Oceans, *122*(2), 1529–1554.

Balwada, D., Smith, K. S., & Abernathey, R. (2018). Submesoscale vertical velocities enhance tracer subduction in an idealized antarctic circumpolar current. *Geophysical Research Letters*, *45*(18), 9790–9802.

Barkan, R., Winters, K. B., & Llewellyn Smith, S. G. (2015). Energy cascades and loss of balance in a reentrant channel forced by wind stress and buoyancy fluxes. *Journal of Physical Oceanography*, *45*(1), 272–293.

Behrenfeld, M. J. (2010). Abandoning sverdrup's critical depth hypothesis on phytoplankton blooms. *Ecology*, *91*(4), 977–989.

Bennington, V., McKinley, G. A., Dutkiewicz, S., & Ullman, D. (2009). What does chlorophyll variability tell us about export and air-sea co2 flux variability in the north atlantic? *Global Biogeochemical Cycles*, *23*(3).

Boccaletti, G., Ferrari, R., & Fox-Kemper, B. (2007). Mixed layer instabilities and restratification. *Journal of Physical Oceanography*, *37*(9), 2228–2250.

Bolton, T., & Zanna, L. (2019). Applications of deep learning to ocean data inference and subgrid parameterization. *Journal of Advances in Modeling Earth Systems*, *11*(1), 376–399.

Bowie, A. R., Lannuzel, D., Remenyi, T. A., Wagener, T., Lam, P. J., Boyd, P. W., ... Trull, T. W. (2009). Biogeochemical iron budgets of the southern ocean south of australia: Decoupling of iron and nutrient cycles in the subantarctic zone by the summertime supply. *Global Biogeochemical Cycles*, *23*(4).

Boyd, P. W., Arrigo, K., Strzepek, R., & Dijken, G. (2012). Mapping phytoplankton iron utilization: Insights into southern ocean supply mechanisms. *Journal of Geophysical Research: Oceans*, *117*(C6).

Boyd, P. W., & Ellwood, M. J. (2010, Sep). The biogeochemical cycle of iron in the ocean. *Nature Geoscience*, *3*(10), 675–682. doi: 10.1038/ngeo964

Brannigan, L., Marshall, D. P., Naveira-Garabato, A., & Nurser, A. G. (2015). The seasonal cycle of submesoscale flows. *Ocean Modelling*, *92*, 69–84.

Brannigan, L., Marshall, D. P., Naveira Garabato, A. C., Nurser, A. G., & Kaiser, J. (2017). Submesoscale instabilities in mesoscale eddies. *Journal of Physical Oceanography*, *47*(12), 3061–3085.

Brown, J. H., Gillooly, J. F., Allen, A. P., Savage, V. M., & West, G. B. (2004). Toward a metabolic theory of ecology. *Ecology*, *85*(7), 1771–1789.

711 Busecke, J. J., & Abernathey, R. P. (2019). Ocean mesoscale mixing linked to cli-
712 mate variability. *Science Advances*, *5*(1), eaav5014.

713 Callies, J., Ferrari, R., Klymak, J. M., & Gula, J. (2015). Seasonality in subme-
714 soscale turbulence. *Nature communications*, *6*, 6862.

715 Callies, J., Flierl, G., Ferrari, R., & Fox-Kemper, B. (2016). The role of mixed-layer
716 instabilities in submesoscale turbulence. *Journal of Fluid Mechanics*, *788*, 5–
717 41.

718 Capet, X., McWilliams, J. C., Molemaker, M. J., & Shchepetkin, A. (2008a).
719 Mesoscale to submesoscale transition in the california current system. part
720 i: Flow structure, eddy flux, and observational tests. *Journal of physical*
721 *oceanography*, *38*(1), 29–43.

722 Capet, X., McWilliams, J. C., Molemaker, M. J., & Shchepetkin, A. (2008b).
723 Mesoscale to submesoscale transition in the california current system. part
724 ii: Frontal processes. *Journal of Physical Oceanography*, *38*(1), 44–64.

725 Capet, X., McWilliams, J. C., Molemaker, M. J., & Shchepetkin, A. (2008c).
726 Mesoscale to submesoscale transition in the california current system. part
727 iii: Energy balance and flux. *Journal of Physical Oceanography*, *38*(10), 2256–
728 2269.

729 Carranza, M. M., & Gille, S. T. (2015). Southern ocean wind-driven entrainment en-
730 hances satellite chlorophyll-a through the summer. *Journal of Geophysical Re-*
731 *search: Oceans*, *120*(1), 304–323.

732 Charney, J. G. (1971). Geostrophic turbulence. *Journal of the Atmospheric Sci-*
733 *ences*, *28*(6), 1087–1095.

734 Chereskin, T. K., Rocha, C. B., Gille, S. T., Menemenlis, D., & Passaro, M. (2019).
735 Characterizing the transition from balanced to unbalanced motions in the
736 southern california current. *Journal of Geophysical Research: Oceans*, *124*(3),
737 2088–2109.

738 Coale, K. H., Johnson, K. S., Chavez, F. P., Buesseler, K. O., Barber, R. T.,
739 Brzezinski, M. A., ... others (2004). Southern ocean iron enrichment ex-
740 periment: carbon cycling in high-and low-si waters. *Science*, *304*(5669),
741 408–414.

742 De Baar, H. J., De Jong, J. T., Bakker, D. C., Löscher, B. M., Veth, C., Bathmann,
743 U., & Smetacek, V. (1995). Importance of iron for plankton blooms and

carbon dioxide drawdown in the southern ocean. *Nature*, *373*(6513), 412.

d'Ovidio, F., Della Penna, A., Trull, T. W., Nencioli, F., Pujol, M.-I., Rio, M.-H., ... Blain, S. (2015). The biogeochemical structuring role of horizontal stirring: Lagrangian perspectives on iron delivery downstream of the kerguelen plateau. *Biogeosciences*, *12*(19), 5567–5581.

Dutkiewicz, S., Follows, M. J., & Bragg, J. G. (2009). Modeling the coupling of ocean ecology and biogeochemistry. *Global Biogeochemical Cycles*, *23*(4).

Ellwood, M. J., Boyd, P. W., & Sutton, P. (2008). Winter-time dissolved iron and nutrient distributions in the subantarctic zone from 40–52s; 155–160e. *Geophysical Research Letters*, *35*(11).

Farneti, R., Delworth, T. L., Rosati, A. J., Griffies, S. M., & Zeng, F. (2010). The role of mesoscale eddies in the rectification of the southern ocean response to climate change. *Journal of Physical Oceanography*, *40*(7), 1539–1557.

Field, C. B., Behrenfeld, M. J., Randerson, J. T., & Falkowski, P. (1998). Primary production of the biosphere: integrating terrestrial and oceanic components. *science*, *281*(5374), 237–240.

Follows, M. J., Dutkiewicz, S., Grant, S., & Chisholm, S. W. (2007). Emergent biogeography of microbial communities in a model ocean. *Science*, *315*(5820), 1843–1846.

Fox-Kemper, B., Danabasoglu, G., Ferrari, R., Griffies, S., Hallberg, R., Holland, M., ... Samuels, B. (2011). Parameterization of mixed layer eddies. iii: Implementation and impact in global ocean climate simulations. *Ocean Modelling*, *39*(1-2), 61–78.

Fox-Kemper, B., & Ferrari, R. (2008). Parameterization of mixed layer eddies. part ii: Prognosis and impact. *Journal of Physical Oceanography*, *38*(6), 1166–1179.

Fox-Kemper, B., Ferrari, R., & Hallberg, R. (2008). Parameterization of mixed layer eddies. part i: Theory and diagnosis. *Journal of Physical Oceanography*, *38*(6), 1145–1165.

Freilich, M. A., & Mahadevan, A. (2019). Decomposition of vertical velocity for nutrient transport in the upper ocean. *Journal of Physical Oceanography*, *49*(6), 1561–1575.

Geider, R. J. (1987). Light and temperature dependence of the carbon to chloro-

phyll a ratio in microalgae and cyanobacteria: implications for physiology and growth of phytoplankton. *New Phytologist*, *106*(1), 1–34.

Gent, P. R. (2016). Effects of southern hemisphere wind changes on the meridional overturning circulation in ocean models. *Annual review of marine science*, *8*, 79–94.

Gent, P. R., & Mcwilliams, J. C. (1990). Isopycnal mixing in ocean circulation models. *Journal of Physical Oceanography*, *20*(1), 150–155.

Giordani, H., & Planton, S. (2000). Modeling and analysis of ageostrophic circulation over the azores oceanic front during the semaphore experiment. *Monthly weather review*, *128*(7), 2270–2287.

Gloege, L., McKinley, G. A., Mouw, C. B., & Ciochetto, A. B. (2017). Global evaluation of particulate organic carbon flux parameterizations and implications for atmospheric pco2. *Global Biogeochemical Cycles*, *31*(7), 1192–1215.

Griffies, S. M., Winton, M., Anderson, W. G., Benson, R., Delworth, T. L., Dufour, C. O., ... others (2015). Impacts on ocean heat from transient mesoscale eddies in a hierarchy of climate models. *Journal of Climate*, *28*(3), 952–977.

Hallberg, R. (2013). Using a resolution function to regulate parameterizations of oceanic mesoscale eddy effects. *Ocean Modelling*, *72*, 92–103.

Hoskins, B. (1982). The mathematical theory of frontogenesis. *Annual review of fluid mechanics*, *14*(1), 131–151.

Hoskins, B., Draghici, I., & Davies, H. (1978). A new look at the ω-equation. *Quarterly Journal of the Royal Meteorological Society*, *104*(439), 31–38.

Jansen, M. F., Adcroft, A. J., Hallberg, R., & Held, I. M. (2015). Parameterization of eddy fluxes based on a mesoscale energy budget. *Ocean Modelling*, *92*, 28–41.

Jiang, M., Measures, C. I., Barbeau, K. A., Charette, M. A., Gille, S. T., Hatta, M., ... others (2019). Fe sources and transport from the antarctic peninsula shelf to the southern scotia sea. *Deep Sea Research Part I: Oceanographic Research Papers*.

Johnson, K. S., Plant, J. N., Coletti, L. J., Jannasch, H. W., Sakamoto, C. M., Riser, S. C., ... others (2017). Biogeochemical sensor performance in the soccom profiling float array. *Journal of Geophysical Research: Oceans*, *122*(8), 6416–6436.

Kitsios, V., Frederiksen, J., & Zidikheri, M. (2013). Scaling laws for parameterisations of subgrid eddy–eddy interactions in simulations of oceanic circulations. *Ocean Modelling*, *68*, 88–105.

Kraichnan, R. H. (1967). Inertial ranges in two-dimensional turbulence. *The Physics of Fluids*, *10*(7), 1417–1423.

Kremer, C. T., Thomas, M. K., & Litchman, E. (2017). Temperature-and size-scaling of phytoplankton population growth rates: Reconciling the eppley curve and the metabolic theory of ecology. *Limnology and Oceanography*, *62*(4), 1658–1670.

Large, W. G., McWilliams, J. C., & Doney, S. C. (1994). Oceanic vertical mixing: A review and a model with a nonlocal boundary layer parameterization. *Reviews of Geophysics*, *32*(4), 363–403.

Lee, E. A., & Kim, S. Y. (2018). Regional variability and turbulent characteristics of the satellite-sensed submesoscale surface chlorophyll concentrations. *Journal of Geophysical Research: Oceans*, *123*(6), 4250–4279.

Lévy, M., Bopp, L., Karleskind, P., Resplandy, L., Éthé, C., & Pinsard, F. (2013). Physical pathways for carbon transfers between the surface mixed layer and the ocean interior. *Global Biogeochemical Cycles*, *27*(4), 1001–1012.

Lévy, M., Ferrari, R., Franks, P. J., Martin, A. P., & Rivière, P. (2012). Bringing physics to life at the submesoscale. *Geophysical Research Letters*, *39*(14).

Lévy, M., Franks, P. J., & Smith, K. S. (2018). The role of submesoscale currents in structuring marine ecosystems. *Nature communications*, *9*(1), 4758.

Lévy, M., Iovino, D., Resplandy, L., Klein, P., Madec, G., Tréguier, A.-M., ... Takahashi, K. (2012). Large-scale impacts of submesoscale dynamics on phytoplankton: Local and remote effects. *Ocean Modelling*, *43*, 77–93.

Lévy, M., Klein, P., & Treguier, A.-M. (2001). Impact of sub-mesoscale physics on production and subduction of phytoplankton in an oligotrophic regime. *Journal of marine research*, *59*(4), 535–565.

Lévy, M., Klein, P., Tréguier, A.-M., Iovino, D., Madec, G., Masson, S., & Takahashi, K. (2010). Modifications of gyre circulation by sub-mesoscale physics. *Ocean Modelling*, *34*(1-2), 1–15.

Levy, M., & Martin, A. (2013). The influence of mesoscale and submesoscale heterogeneity on ocean biogeochemical reactions. *Global Biogeochemical Cycleso*,

27(4), 1139–1150.

Lévy, M., Resplandy, L., Klein, P., Capet, X., Iovino, D., & Éthé, C. (2012). Grid degradation of submesoscale resolving ocean models: Benefits for offline passive tracer transport. *Ocean Modelling*, *48*, 1–9.

Leymarie, E., Penkerc'h, C., Vellucci, V., Lerebourg, C., Antoine, D., Boss, E., ... Claustre, H. (2018). Proval: A new autonomous profiling float for high quality radiometric measurements. *Frontiers in Marine Science*, *5*, 437.

Liang, X., Piecuch, C. G., Ponte, R. M., Forget, G., Wunsch, C., & Heimbach, P. (2017). Change of the global ocean vertical heat transport over 1993–2010. *Journal of Climate*, *30*(14), 5319–5327.

Liang, X., Wunsch, C., Heimbach, P., & Forget, G. (2015). Vertical redistribution of oceanic heat content. *Journal of Climate*, *28*(9), 3821–3833.

Llort, J., Langlais, C., Matear, R., Moreau, S., Lenton, A., & Strutton, P. G. (2018). Evaluating southern ocean carbon eddy-pump from biogeochemical-argo floats. *Journal of Geophysical Research: Oceans*, *123*(2), 971–984.

Llort, J., Lévy, M., Sallée, J.-B., & Tagliabue, A. (2015). Onset, intensification, and decline of phytoplankton blooms in the southern ocean. *ICES Journal of Marine Science: Journal du Conseil*, *72*(6), 1971–1984.

Llort, J., Lévy, M., Sallée, J.-B., & Tagliabue, A. (2019). Nonmonotonic response of primary production and export to changes in mixed-layer depth in the southern ocean. *Geophysical Research Letters*, *46*(6), 3368–3377.

Mack, S. L., Dinniman, M. S., McGillicuddy Jr, D. J., Sedwick, P. N., & Klinck, J. M. (2017). Dissolved iron transport pathways in the ross sea: Influence of tides and horizontal resolution in a regional ocean model. *Journal of Marine Systems*, *166*, 73–86.

Mahadevan, A. (2016). The impact of submesoscale physics on primary productivity of plankton. *Annual review of marine science*, *8*, 161–184.

Marshall, J., Hill, C., Perelman, L., & Adcroft, A. (1997). Hydrostatic, quasi-hydrostatic, and nonhydrostatic ocean modeling. *Journal of Geophysical Research: Oceans*, *102*(C3), 5733-5752.

Martin, J. H., Gordon, R. M., & Fitzwater, S. E. (1990). Iron in antarctic waters. *Nature*, *345*(6271), 156.

McDougall, T. J., & McIntosh, P. C. (2001). The temporal-residual-mean veloc-

876 ity. part ii: Isopycnal interpretation and the tracer and momentum equations.
877 *Journal of Physical Oceanography*, *31*(5), 1222–1246.
878 McGillicuddy, D. J., Sedwick, P. N., Dinniman, M. S., Arrigo, K. R., Bibby, T. S.,
879 Greenan, B. J., ... others (2015). Iron supply and demand in an antarctic
880 shelf ecosystem. *Geophysical Research Letters*, *42*(19), 8088–8097.
881 McWilliams, J. C. (2016). Submesoscale currents in the ocean. *Proc. R. Soc. A*,
882 *472*(2189), 20160117.
883 McWilliams, J. C., Gula, J., & Molemaker, M. J. (2019). The gulf stream north
884 wall: Ageostrophic circulation and frontogenesis. *Journal of Physical Oceanog-*
885 *raphy*, *49*(4), 893–916.
886 Molemaker, M. J., McWilliams, J. C., & Capet, X. (2010). Balanced and unbalanced
887 routes to dissipation in an equilibrated eady flow. *Journal of Fluid Mechanics*,
888 *654*, 35–63.
889 Molemaker, M. J., McWilliams, J. C., & Yavneh, I. (2005). Baroclinic instability
890 and loss of balance. *Journal of Physical Oceanography*, *35*(9), 1505–1517.
891 Moore, C., Mills, M., Arrigo, K., Berman-Frank, I., Bopp, L., Boyd, P., ... oth-
892 ers (2013). Processes and patterns of oceanic nutrient limitation. *Nature*
893 *geoscience*, *6*(9), 701.
894 Moore, J. K., & Abbott, M. R. (2000). Phytoplankton chlorophyll distributions and
895 primary production in the southern ocean. *Journal of Geophysical Research:*
896 *Oceans*, *105*(C12), 28709–28722.
897 Moore, J. K., Doney, S. C., & Lindsay, K. (2004). Upper ocean ecosystem dynam-
898 ics and iron cycling in a global three-dimensional model. *Global Biogeochemical*
899 *Cycles*, *18*(4).
900 Moore, J. K., Lindsay, K., Doney, S. C., Long, M. C., & Misumi, K. (2013). Marine
901 ecosystem dynamics and biogeochemical cycling in the community earth sys-
902 tem model [cesm1 (bgc)]: Comparison of the 1990s with the 2090s under the
903 rcp4. 5 and rcp8. 5 scenarios. *Journal of Climate*, *26*(23), 9291–9312.
904 Nicholson, S.-A., Lévy, M., Llort, J., Swart, S., & Monteiro, P. (2016). Investigation
905 into the impact of storms on sustaining summer primary productivity in the
906 sub-antarctic ocean. *Geophysical Research Letters*, *43*(17), 9192–9199.
907 Nishioka, J., Obata, H., & Tsumune, D. (2013). Evidence of an extensive spread of
908 hydrothermal dissolved iron in the indian ocean. *Earth and Planetary Science*

Letters, *361*, 26–33.

Nolting, R., Gerringa, L., Swagerman, M., Timmermans, K., & De Baar, H. (1998). Fe (iii) speciation in the high nutrient, low chlorophyll pacific region of the southern ocean. *Marine Chemistry*, *62*(3-4), 335–352.

Pearson, B., Fox-Kemper, B., Bachman, S., & Bryan, F. (2017). Evaluation of scale-aware subgrid mesoscale eddy models in a global eddy-rich model. *Ocean Modelling*, *115*, 42–58.

Qiu, B., Chen, S., Klein, P., Sasaki, H., & Sasai, Y. (2014). Seasonal mesoscale and submesoscale eddy variability along the north pacific subtropical countercurrent. *Journal of Physical Oceanography*, *44*(12), 3079–3098.

Renault, L., Molemaker, M. J., Gula, J., Masson, S., & McWilliams, J. C. (2016). Control and stabilization of the gulf stream by oceanic current interaction with the atmosphere. *Journal of Physical Oceanography*, *46*(11), 3439–3453.

Riser, S. C., Swift, D., & Drucker, R. (2018). Profiling floats in soccom: Technical capabilities for studying the southern ocean. *Journal of Geophysical Research: Oceans*.

Rocha, C. B., Gille, S. T., Chereskin, T. K., & Menemenlis, D. (2016). Seasonality of submesoscale dynamics in the kuroshio extension. *Geophysical Research Letters*, *43*(21), 11–304.

Rosso, I., Hogg, A. M., Matear, R., & Strutton, P. G. (2016). Quantifying the influence of sub-mesoscale dynamics on the supply of iron to southern ocean phytoplankton blooms. *Deep Sea Research Part I: Oceanographic Research Papers*, *115*, 199–209.

Rosso, I., Hogg, A. M., Strutton, P. G., Kiss, A. E., Matear, R., Klocker, A., & van Sebille, E. (2014). Vertical transport in the ocean due to sub-mesoscale structures: Impacts in the kerguelen region. *Ocean Modelling*, *80*, 10–23.

Sasaki, H., Klein, P., Qiu, B., & Sasai, Y. (2014). Impact of oceanic-scale interactions on the seasonal modulation of ocean dynamics by the atmosphere. *Nature communications*, *5*, 5636.

Schoonover, J., Dewar, W. K., Wienders, N., & Deremble, B. (2017). Local sensitivities of the gulf stream separation. *Journal of Physical Oceanography*, *47*(2), 353–373.

Sinha, A., & Abernathey, R. P. (2016). Time scales of southern ocean eddy equili-

bration. *Journal of Physical Oceanography*, *46*(9), 2785–2805.

Smith, K. M., Hamlington, P. E., & Fox-Kemper, B. (2016). Effects of submesoscale turbulence on ocean tracers. *Journal of Geophysical Research: Oceans*, *121*(1), 908–933.

Song, H., Long, M. C., Gaube, P., Frenger, I., Marshall, J., & McGillicuddy Jr, D. J. (2018). Seasonal variation in the correlation between anomalies of sea level and chlorophyll in the antarctic circumpolar current. *Geophysical Research Letters*, *45*(10), 5011–5019.

Song, H., Marshall, J., Munro, D. R., Dutkiewicz, S., Sweeney, C., McGillicuddy, D. J., & Hausmann, U. (2016). Mesoscale modulation of air-sea co2 flux in drake passage. *Journal of Geophysical Research: Oceans*, *121*(9), 6635–6649.

Su, Z., Wang, J., Klein, P., Thompson, A. F., & Menemenlis, D. (2018). Ocean submesoscales as a key component of the global heat budget. *Nature communications*, *9*(1), 775.

Swart, S., Thomalla, S., & Monteiro, P. (2015). The seasonal cycle of mixed layer dynamics and phytoplankton biomass in the sub-antarctic zone: A high-resolution glider experiment. *Journal of Marine Systems*, *147*, 103–115.

Tagliabue, A., Mtshali, T., Aumont, O., Bowie, A. R., Klunder, M. B., Roychoudhury, A. N., & Swart, S. (2012). A global compilation of dissolved iron measurements: focus on distributions and processes in the southern ocean. *Biogeosciences*, *9*(6), 2333–2349.

Tagliabue, A., Sallée, J.-B., Bowie, A. R., Lévy, M., Swart, S., & Boyd, P. W. (2014). Surface-water iron supplies in the southern ocean sustained by deep winter mixing. *Nature Geoscience*, *7*(4), 314–320.

Uchida, T., Abernathey, R., & Smith, S. (2017). Seasonality of eddy kinetic energy in an eddy permitting global climate model. *Ocean Modelling*, *118*, 41–58.

Uchida, T., Balwada, D., Abernathey, R., Prend, C., Boss, E., & Gille, S. (submitted). Southern ocean phytoplankton blooms observed by biogeochemical floats. *Journal of Geophysical Research: Oceans*.

Vallis, G. K. (2017). *Atmospheric and oceanic fluid dynamics*. Cambridge University Press.

Verdy, A., & Mazloff, M. (2017). A data assimilating model for estimating southern ocean biogeochemistry. *Journal of Geophysical Research: Oceans*, *122*(9),

6968–6988.

Wadley, M. R., Jickells, T. D., & Heywood, K. J. (2014). The role of iron sources and transport for southern ocean productivity. *Deep Sea Research Part I: Oceanographic Research Papers*, *87*, 82–94.

Westberry, T., Behrenfeld, M., Siegel, D., & Boss, E. (2008). Carbon-based primary productivity modeling with vertically resolved photoacclimation. *Global Biogeochemical Cycles*, *22*(2).

Wolfe, C., Cessi, P., McClean, J., & Maltrud, M. (2008). Vertical heat transport in eddying ocean models. *Geophysical Research Letters*, *35*(23).

Zhang, Z., Qiu, B., Klein, P., & Travis, S. (2019). The influence of geostrophic strain on oceanic ageostrophic motion and surface chlorophyll. *Nature Communications*, *10*(1), 2838.

Zika, J. D., Le Sommer, J., Dufour, C. O., Molines, J.-M., Barnier, B., Brasseur, P., ... others (2013). Vertical eddy fluxes in the southern ocean. *Journal of Physical Oceanography*, *43*(5), 941–955.

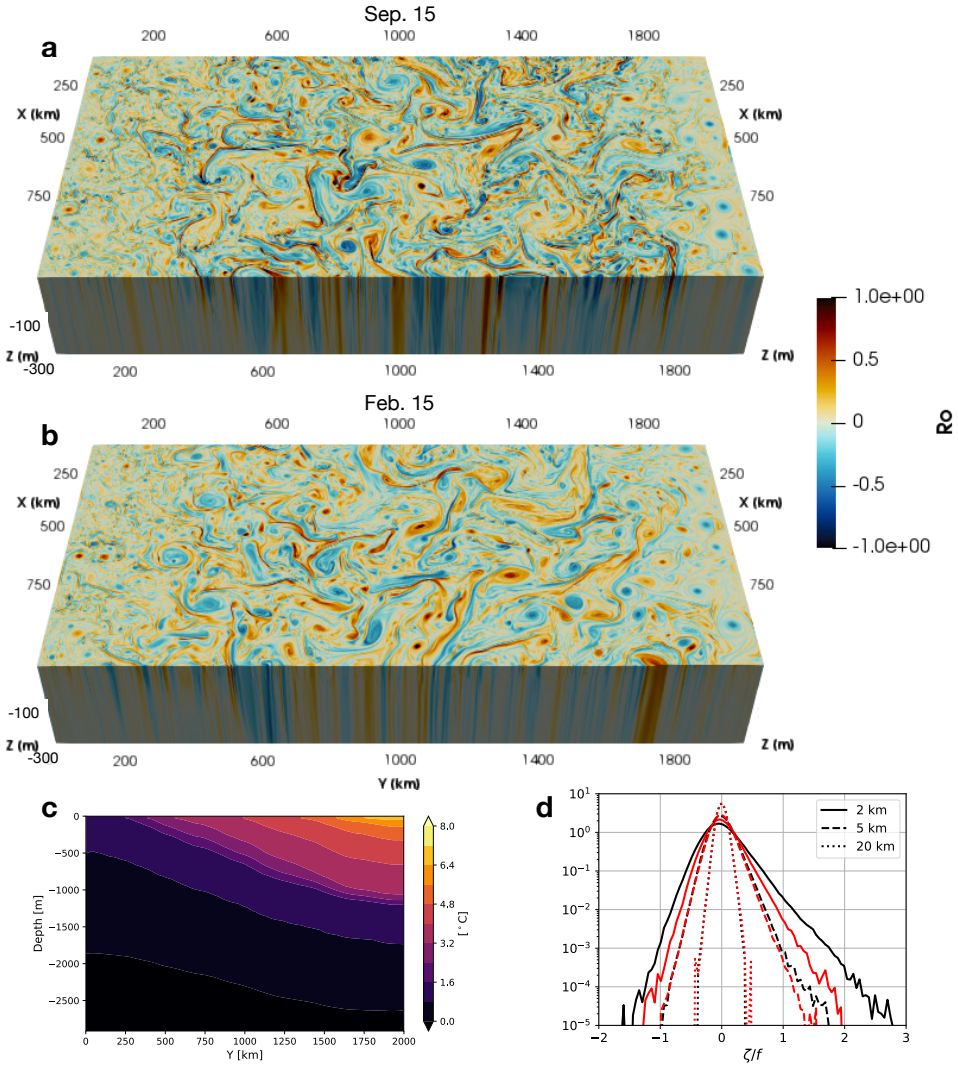

Figure 1. Relative vorticity normalized by the local Coriolis parameter (Ro $= \frac{\zeta}{f}$) for the 2 km run on September 15 **a** and February 15 **b** in the top 300 m. **c** The zonal-annual mean stratification from the 2 km run plotted against depth and meridional distance. **d** Seasonal probability density function of Ro for each resolution is shown in. Winter (July, August, September) is shown in black and summer (January, February, March) in red.

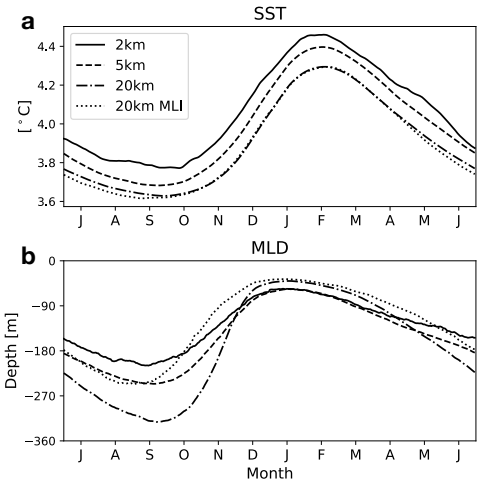

Figure 2. The spatial average over the meridional extent of $y \in [600, 1400]$ km of daily-averaged SST from the 2 km run **a**. Note that the month axis starts from July, austral winter. **b** The spatial mean of daily-averaged MLD for each run.

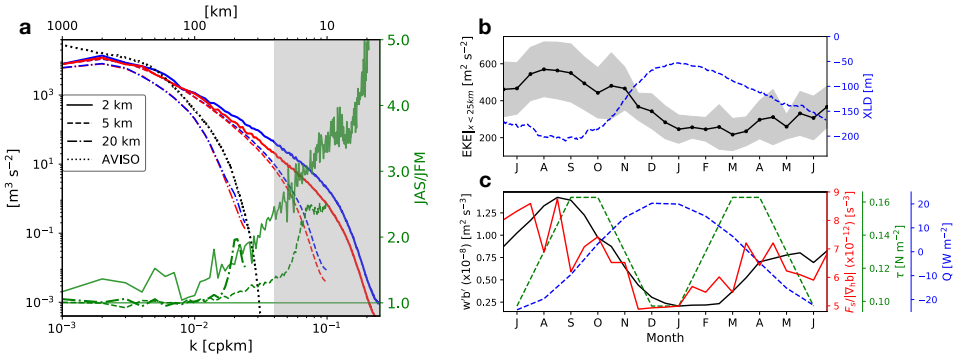

Figure 3. Seasonal and meridional mean of the zonal wavenumber KE power spectra for the 2 km (solid), 5 km (dashed) and non-parametrized 20 km run (dotted-dash), and climatology of AVISO (dotted) **a**. The x axis at the top shows the wavelength each wavenumber corresponds to. Red (blue) indicates winter (summer). The green lines show the ratio of austral winter over summer for the 2 km (solid), 5 km (dashed), and 20 km run (dotted-dash) and the grey shading shows scales below 25 km. **b** The time series of surface KE at scales smaller than 25 km and MLD (blue dashed) depth averaged over the top 100 m from the 2 km run. **c** Baroclinic energy conversion rate (black solid) and frontogenesis function (red solid) depth averaged over the top 100 m, surface wind stress (green dashed) and heat flux (orange dashed).

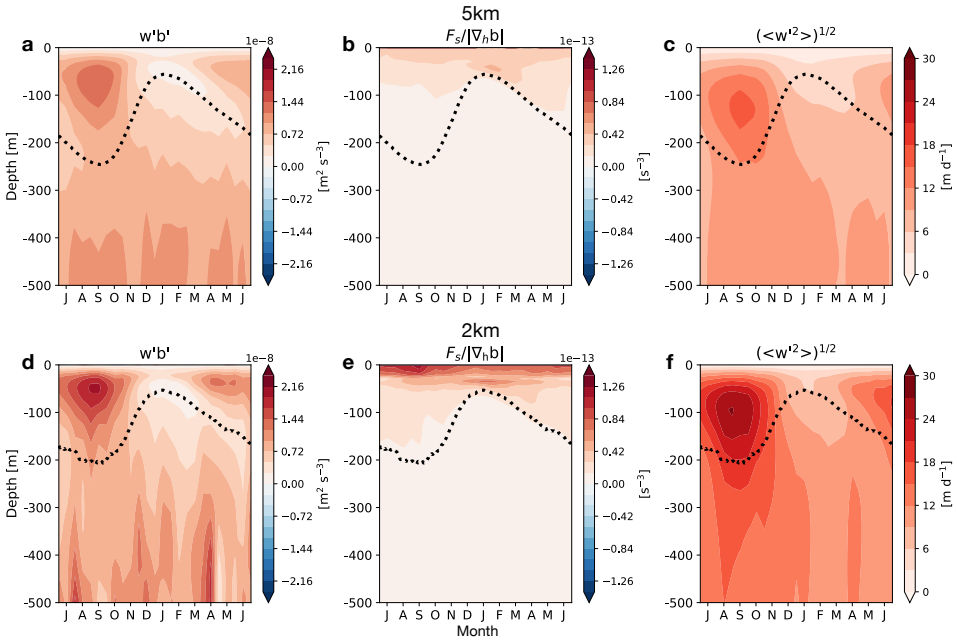

Figure 4. Hovmöller diagram of baroclinic energy conversion rate ($w'b'$) averaged spatially over $y \in [600, 1400]$ km (**a**,**d**). **b**,**e** Monthly climatology of the frontogenesis function normalized by the horizontal buoyancy gradient in [s^{-3}], and root-mean square of w [m d^{-1}] (**c**,**f**). Each variable is shown for the two resolution 5 and 2 km runs and MLD in black dotted lines.

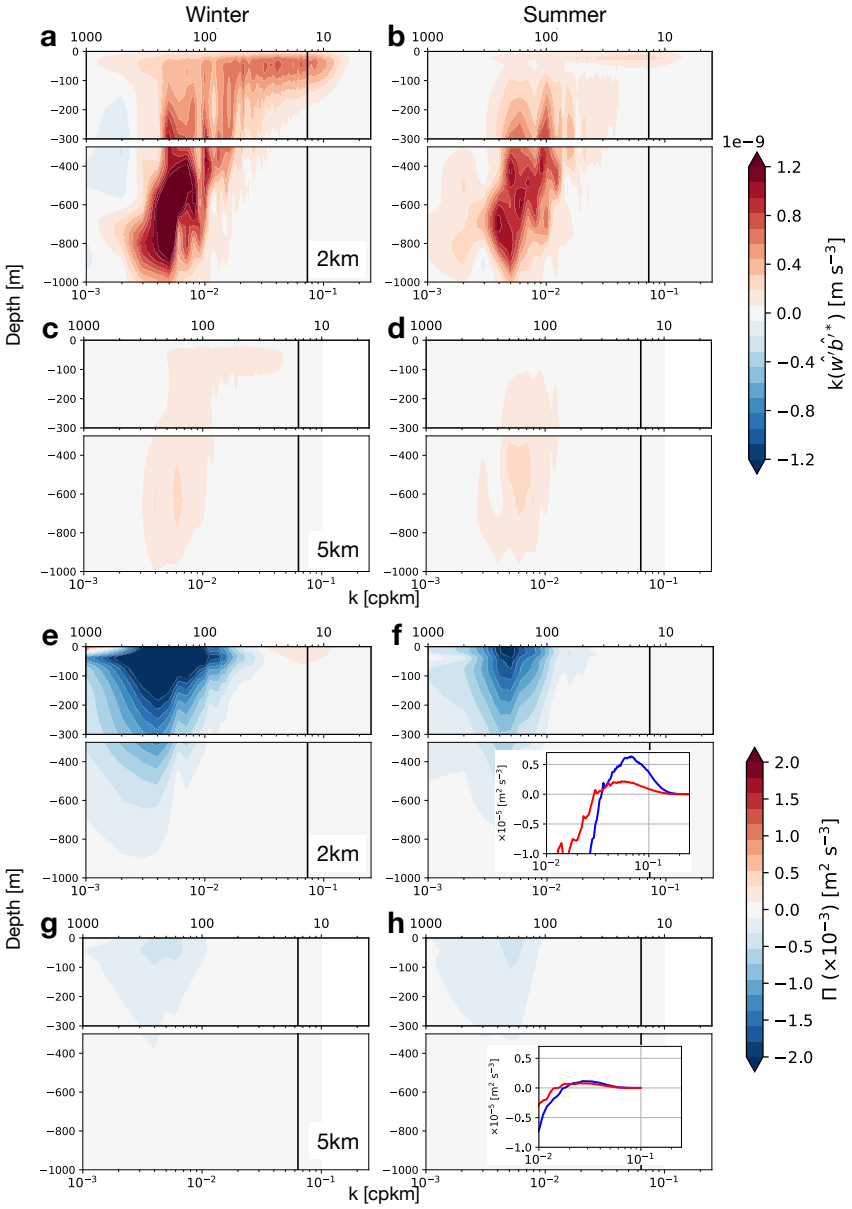

Figure 5. Seasonal-meridional mean over $y \in [600, 1400]$ km of the zonal-wavenumber cross spectra of vertical velocity and buoyancy ($\mathcal{R}[\hat{w}'\hat{b}'^{*}(k)]$) in variance preserving form for winter **a** and summer **b** for the 2- and 5-km (**c**,**d**) run. The spatial scale corresponding to each wavenumber is shown on the top x axes of each panel in [km]. **e-h** The spectral flux of total KE ($\Pi(k)$) is shown in the same manner. The black solid lines show the Rossby deformation wavenumber. The lower-right panel is a zoomed-in figure of the KE cascade at scales below 100 km averaged over the top 100 m with winter (summer) shown in blue (red).

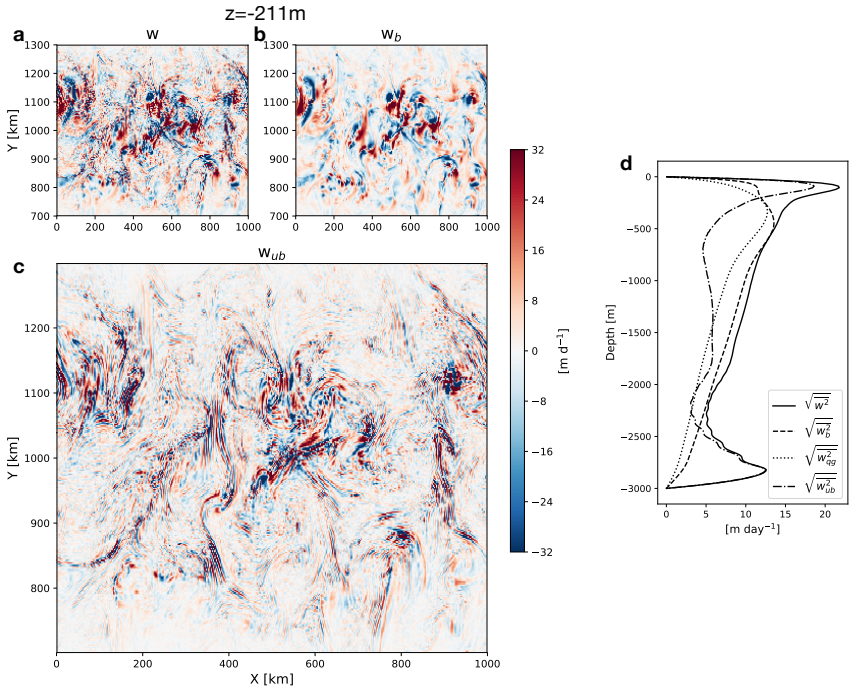

Figure 6. Snapshot of the total vertical velocity (w; **a**) on August 15, balanced (w_b; **b**) and unbalanced (w_ub; **c**) at the depth of $z = -211$ m. **d** The vertical profile of the root-mean square of each term along with an inversion using quasi-geostrophic approximation (w_qg). The overbar ($\bar{\cdot}$) indicates the spatial averaging.

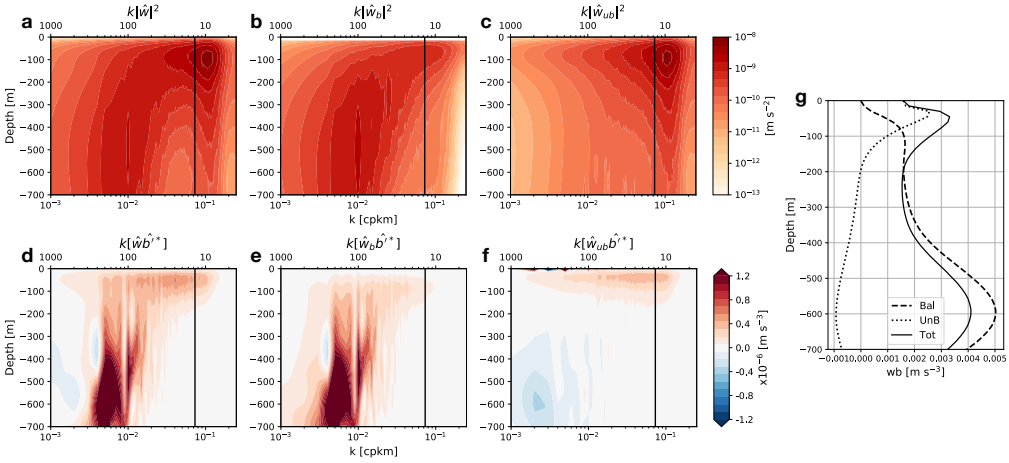

Figure 7. The zonal wavenumber power spectra of total vertical velocity (w; **a**), balanced (w_b; **b**) and unbalanced (w_ub; **c**) in variance preserving form. The spatial scales corresponding to the wavenumbers are again shown on the top x axes in [km]. **d-f** Zonal wavenumber cross spectra of vertical velocity and buoyancy ($\mathcal{R}[\hat{w}\hat{b}'^*]$) in the same manner. The black solid lines show the Rossby deformation wavenumber. **g** Profile of vertical buoyancy flux associated with each component.

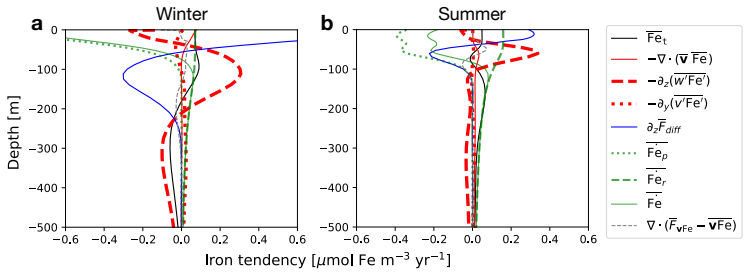

Figure 8. The iron budget for winter (July, August, September; **a**) and summer (January, February, March; **b**) over the meridional extent of $y \in [600, 1400]$ km from the 2 km run. The residual term in grey dashed lines comes from the tracer advective flux scheme which prevents tracer concentrations from taking negative values.

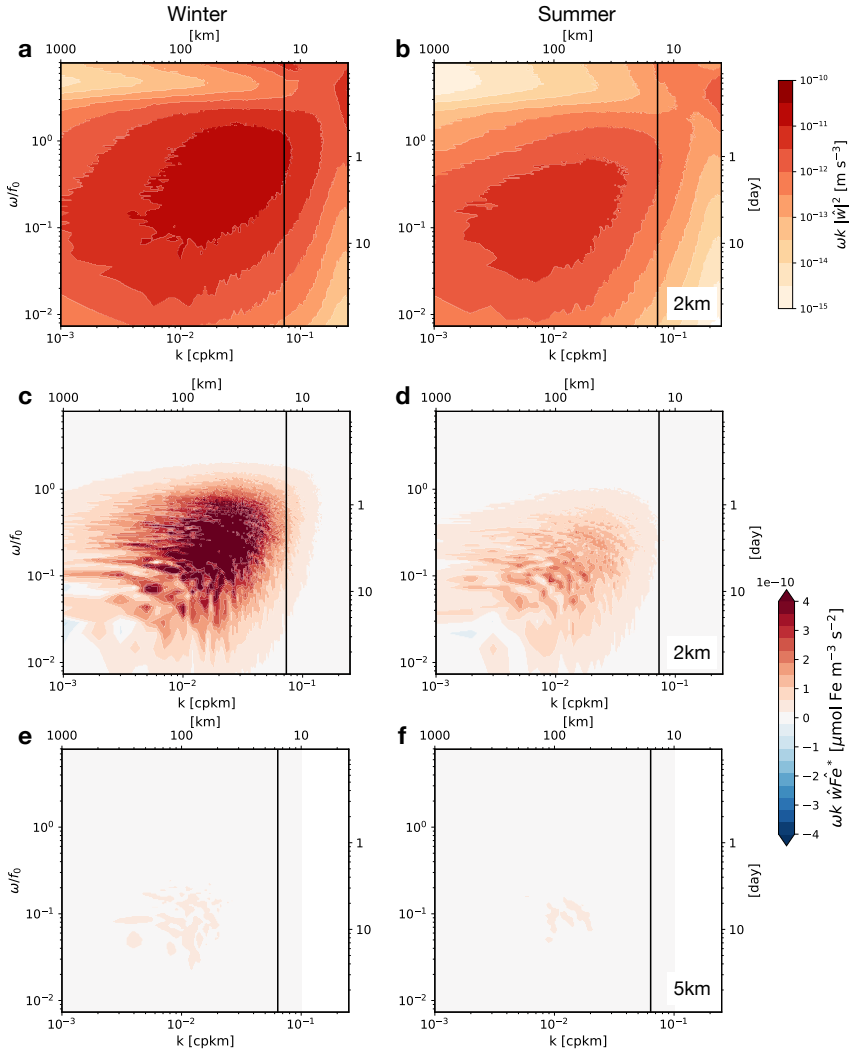

Figure 9. Frequency-zonal wavenumber power spectra of w (**a**,**b**) and cross spectra of w and Fe (**c**,**d**) in variance preserving form from the 2-km run at $z = -211$ m depth using hourly snapshot outputs for winter (July, August, September; left) and summer (January, February, March; right). Cross spectra for the 5-km run are shown in **e**,**f**. Frequency is normalized by the Coriolis parameter at the center of the domain. The top and right x-y axes in each panel show the corresponding spatial scale in [km] and dimensionalized frequency in the units of [day]. The spectra were averaged over the meridional extent $y \in [600, 1400]$ km. The black solid lines show the Rossby deformation wavenumber.

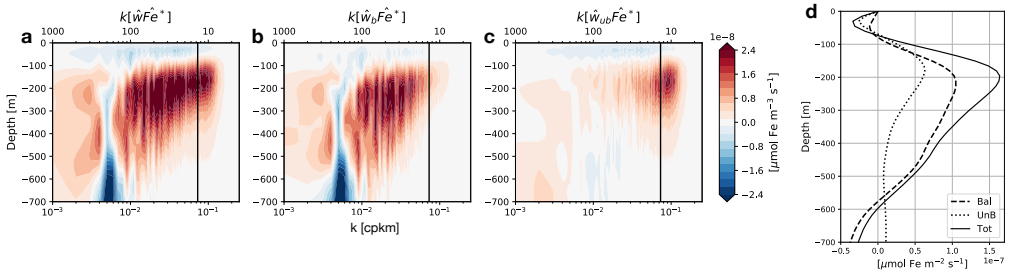

Figure 10. The variance preserving zonal-wavenumber cross spectra of vertical velocity and iron averaged over the meridional extent of $y \in [800, 1200]$ km and winter (JAS) for total **a**, balanced **b**, and unbalanced vertical velocity **c**. The black solid lines show the Rossby deformation wavenumber. **d** The vertical profile of iron transport attributed to each component.

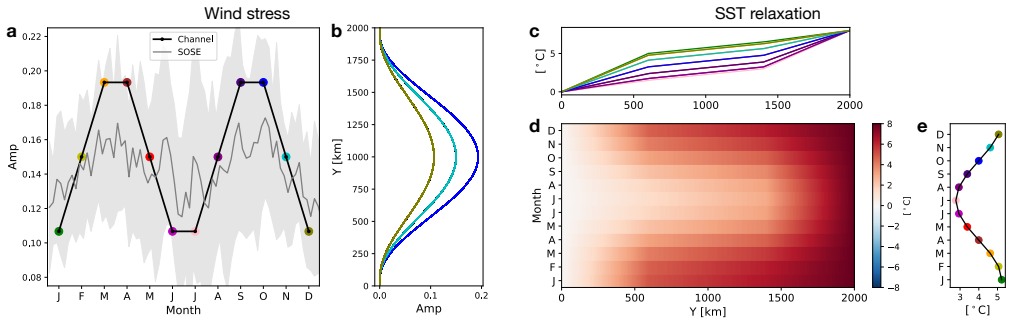

Figure A1. The monthly surface wind stress amplitude for each month in our model is plotted against the annual climatology of the Southern Ocean State Estimate (?, ?, SOSE;)]verdy2017data wind stress averaged zonally between 50-56S **a**. The grey shadings are the standard deviation of SOSE. **b** The meridional profile of our westerly jet with the colors corresponding to them in panel **a**. **d** SST relaxation profiles are plotted against month and meridional extent and panel **c** is showing the same thing along temperature and meridional extent. **e** The meridional average of **c** with colors corresponding with each other.

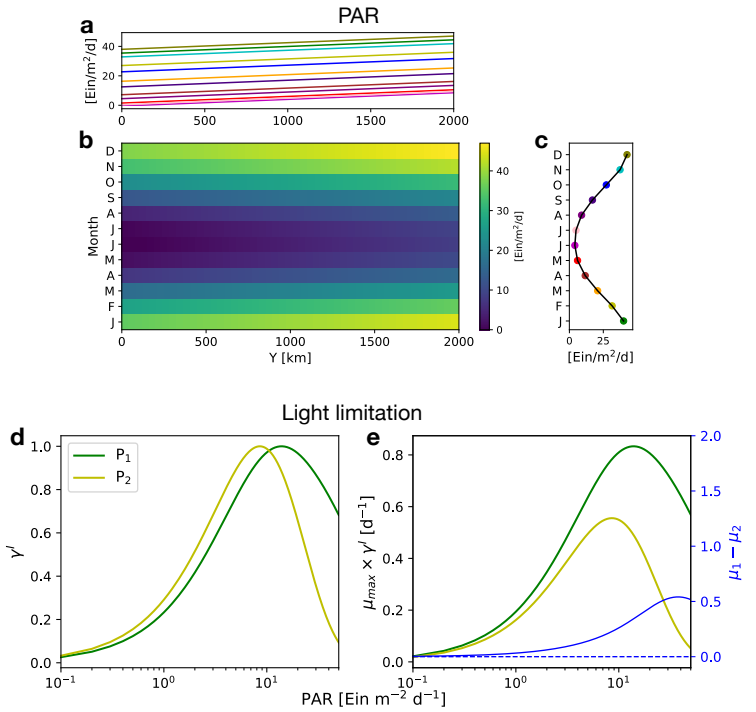

Figure A2. Surface PAR in our runs plotted against month and meridional extent **b**. **c** The meridional mean of **a** and **b** with the colors of **a** and **c** correspond with each other. **d** The light limitation factor for each plankton (eqn. A2; Diatoms (P_1) in green and small phytoplankton (P_2) in yellow) and it multiplied by the maximum growth rate in **e**. The blue line shows the difference between the two ($\mu_1 - \mu_2$).

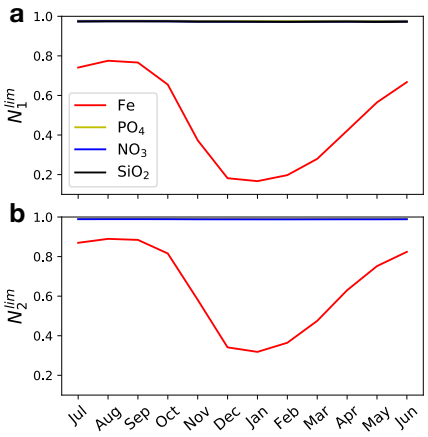

Figure A3. Nutrient limitation factor (eqn. A4) for diatoms ($i = 1$; **a**) and small phytoplankton ($i = 2$; **b**) using monthly-mean nutrient outputs from the 2 km run averaged over the top 100 m.

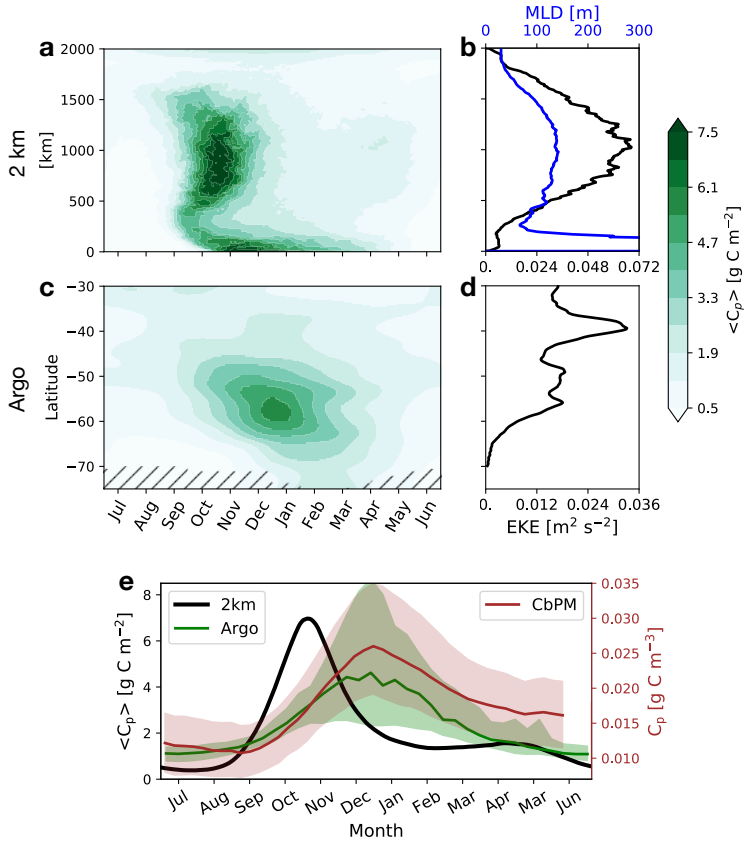

Figure B1. Hovmöller diagram of $\langle C_p \rangle$ for the 2 km run **a**, and from BGC Argo floats **c**. The hatch indicates grids where there were less than 10 Argo profiles over the five years of deployment by SOCCOM and SOCLIM. **b**,**d** Zonal mean of surface KE and MLD from the 2 km run and AVISO plotted against meridional axes. **e** Spatial and daily median of $\langle C_p \rangle$ for the 2 km run between $y \in [600, 1400]$ km (black), 10-daily median BGC Argo (green), and eight-day averaged C_p outputs from CbPM (brown) between 45S-60S. Note the difference in the units. As CbPM relies on satellite Chlorophyll observations, the month of June lacks data due to poor light conditions. The green and brown shading indicated the zonal and daily interquartile range.